

Effects of Inaccurate Response Function Calibration on Characteristics of the Fiber Orientation Distribution in Diffusion MRI

**Fenghua Guo^{1*}, Chantal M.W. Tax², Alberto De Luca¹, Max A. Viergever¹,
Anneriet Heemskerk¹, Alexander Leemans¹**

¹Image Sciences Institute, University Medical Center Utrecht, Utrecht University, Utrecht, the Netherlands

²Cardiff University Brain Research Imaging Centre, School of Psychology, Cardiff University, United Kingdom

* Correspondence should be addressed to:

Fenghua Guo

Image Sciences Institute
University Medical Center Utrecht
Heidelberglaan 100
Room Q.02.4.45
3584CX Utrecht
The Netherlands

Tel: +31 88 75 57772

Email: f.guo@umcutrecht.nl

Abstract

1
2 Diffusion MRI of the brain enables to quantify white matter fiber orientations noninvasively.
3 Several approaches have been proposed to estimate such characteristics from diffusion MRI
4 data with spherical deconvolution being one of the most widely used methods. Constrained
5 spherical deconvolution requires to define – or derive from the data – a response function,
6 which is used to compute the fiber orientation distribution (FOD). This definition or derivation
7 is not unequivocal and can thus result in different characteristics of the response function which
8 are expected to affect the FOD computation and the subsequent fiber tracking. In this work,
9 we explored the effects of inaccuracies in the shape and scaling factors of the response
10 function on the FOD characteristics. With simulations, we show that underestimation of the
11 shape factor in the response functions has a larger effect on the FOD peaks than
12 overestimation of the shape factor, whereas the latter will cause more spurious peaks.
13 Moreover, crossing fiber populations with a smaller separation angle were more sensitive to
14 the response function inaccuracy than fiber populations with more orthogonal separation
15 angles. Furthermore, the FOD characteristics show deviations as a result of modified shape
16 and scaling factors of the response function. Results with the in vivo data demonstrate that the
17 deviations of the FODs and spurious peaks can further deviate the termination of propagation
18 in fiber tracking. This work highlights the importance of proper definition of the response
19 function and how specific calibration factors can affect the FOD and fiber tractography results.
20

21 **Keywords:** Diffusion MRI; constrained spherical deconvolution (CSD); response function; fiber
22 orientation distribution (FOD); brain fiber tractography; apparent fiber density (AFD).

23

24 1. Introduction

25

26 Diffusion MRI allows to characterize tissue microstructure in vivo and noninvasively by
27 measuring the anisotropic diffusion of water molecules [1,2]. Diffusion tensor imaging (DTI) [3]
28 is the most widely used model in clinical studies to relate the diffusion MRI signals to the
29 diffusion characteristics of the underlying tissue. However, DTI is inadequate to estimate the
30 directional information in voxels containing crossing fibers [4,5]. A commonly used approach
31 to resolve more complex fiber configurations in the brain is spherical deconvolution (SD) [6–
32 8]. SD also allows for the extraction of fiber population specific microstructural measures
33 derived from the magnitudes of the fiber orientation distribution (FOD) functions, such as
34 apparent fiber density (AFD) [9] and hindrance modulated orientational anisotropy (HMOA)
35 [10].

36 SD requires an appropriate response function as input to estimate the FOD [7]. The
37 response function, representing the diffusion signal for a single fiber population, is ideally
38 calibrated from the acquired diffusion MRI data [11,12]. In brief, for each subject, the voxels
39 containing only single fiber populations are localized, and an average of the diffusivity
40 characteristics within those voxels is used to represent the subject specific response function.
41 An inadequately chosen response function can affect the quantification of FOD characteristics
42 like AFD and HMOA, as well as the fiber tractography.

43 In order to compare inter-subject AFD, Raffelt and colleagues [9] chose a response
44 function common to all subjects to minimize the differences between subjects for voxel-wise
45 AFD comparison. However, this may potentially result in a bias in the estimated FOD.
46 Specifically, the use of such a common response function for group-wise analysis may cause
47 biases in the FOD peak orientations for individual subjects. Therefore, whereas a common
48 response function is optimal for the comparison of AFD and HMOA in group studies [9], it is
49 unclear whether this is also optimal for group-wise tractography studies because of the
50 potentially inaccurate FOD peak orientations and concomitant spurious FOD peaks. Intuitively,
51 the difference in response function characteristics across healthy subjects are not expected to

52 be large, as response functions are generally averaged from more than hundreds of voxels
53 that are supposed to contain single fiber populations [6,7,12]. This was partly demonstrated by
54 Jeurissen and colleagues [13], who studied the inter-subject response functions of 100 healthy
55 subjects from the Human Connectome Project (HCP) [14] and observed only subtle
56 differences. Accordingly, it seems justified not to be too concerned about inter-subject
57 response function variability in healthy subjects, since either using averaged response
58 functions or individual response functions is not likely to affect the FOD profiles in the HCP
59 dataset. However, although the differences in the response functions of healthy subjects may
60 be small [13], this is likely not the case for subjects with some form of pathology. The inter-
61 subject signal deviations do raise concern for aging and diseased groups.

62 White matter degeneration, whether caused by aging or by a disease process, may
63 substantially alter the response function. Hence, studying subjects of different ages with a
64 common response function might introduce errors due to discrepancies in white matter
65 characteristics. Therefore as the focus of this work, it is useful to investigate such differences
66 in response functions and the resulting variations of the FOD. A thorough numerical evaluation
67 focusing on the angular characteristics of FOD is needed to shed more light on this issue.

68 Previous studies have discussed the effect of improperly calibrated response functions
69 on the FOD characteristics and fiber tracking. Tournier [7] and Dell'Acqua [8] reasoned from a
70 mathematical point of view that a wrongly chosen response function would affect the
71 magnitudes of FOD peaks, thus also AFD and HMOA, but would leave their orientations
72 unaffected. Dell'Acqua and colleagues [8,10] investigated with simulations and in vivo data the
73 effects of various response function changes on the FOD profiles, including variations in the
74 response function shape and scaling factor, as well as in axonal radius and in angle of crossing
75 pathways for the damped Richardson-Lucy (dRL) method. Their paper focused on the effect
76 of the response function on FOD amplitudes and the sensitivity of HMOA to diffusivity changes
77 per fiber population, as compared to traditional metrics as fractional anisotropy (FA) and mean
78 diffusivity (MD). Parker [15] studied the FOD peak orientations and the existence of spurious
79 peaks in simulations as a function of the response function miscalibration for CSD and dRL.

80 The results of that study demonstrate that sharper response functions resulted in more
81 spurious peaks in the FOD profiles, and that the mismatch of the calibrated-targeted response
82 functions introduced uncertainty on the main FOD peak orientations. However, in previous
83 work[15], the authors used the FA value as a metric to characterize the response functions, a
84 strategy which is unable to describe the true axial and radial diffusivities in crossing fibers [16].
85 Changes in FA entangle changes in the axial and radial diffusivities, so that the effects on
86 these two diffusivities could not be studied straightforwardly. Here we seek to disentangle
87 these effects and, complementing earlier studies [15,17], also aim to quantify both the effect
88 on peak magnitude and angular deviation.

89 In this manuscript we studied how variations in the response function affect voxel-wise
90 FOD characteristics and fiber tracking. Changes in pathology are likely reflected in changes in
91 either the axial or the radial diffusivity, which in our study, is represented by the shape and
92 scale factor of the response function. Simulations were designed to explore the effects of the
93 response function shape and scaling factor on the FOD properties, such as the number of FOD
94 peaks, their orientation (for tractography) and magnitude, and the AFD. Additionally, in vivo
95 data from the Human Connectome Project (HCP) were used to illustrate how the choice of the
96 response function in CSD can affect the FOD quantification and fiber tracking.

97

98 **2. Methods**

99

100 In Sections 2.1 and 2.2, we give a brief background on (constrained) spherical
101 deconvolution methods to reconstruct the FOD. In Section 2.3 we outline the simulation
102 experiments and introduce the shape and scaling factor that characterize the response
103 function. Section 2.4 presents the parameter settings used in these simulations. In Section 2.5,
104 the in vivo data experiments are described.

105

106 **2.1 Constrained Spherical Deconvolution**

107

108 Recent studies showed that crossing fibers account for over 90% of white matter voxels
109 [4]. The DTI representation cannot resolve crossing fibers by design and thus provides non-
110 specific metrics in such voxels. Spherical deconvolution approaches [6–8,18,19] overcome this
111 limitation and allow for estimating the FOD for more complex fiber configurations, while
112 retaining reasonable computation and acquisition time compared with other methods [20–23].

113 CSD assumes that the diffusion MRI signals can be expressed as the spherical
114 convolution of a fiber response function with the FODs in the spherical harmonics basis, thus
115 also assuming the validity of the response function in all voxels. The response function
116 represents the diffusion-weighted signal of a single fiber population. Spherical harmonics form
117 a complete basis on the sphere. However, to fully reconstruct a signal on the sphere, the
118 spherical harmonics should have infinite order, which is not possible in practice. In clinical
119 studies, signals with up to 60 gradient directions are generally acquired, limiting the order of
120 the spherical harmonics to 8, which we also adopted in this work.

121 The FODs are used to infer information on the orientation of the fiber pathways under
122 the assumption that the FOD peak orientations coincide with the underlying fiber directions.
123 To reconstruct the FOD, truncation of the spherical harmonics is needed, causing the so-called
124 “ringing” effect on the FOD profiles, which introduces implausible negative values. In order to
125 suppress the ringing effect and the sensitivity to noise, the regularization of FOD was proposed

126 [7,19,24] to improve the conditioning of the deconvolution problem, which is further referred to
127 as constrained SD (i.e., CSD). In addition to directional information, the magnitudes of the FOD
128 are used to compute additional metrics, such as AFD [9] and HMOA [10]. The accurate
129 estimation of FOD peak directions and magnitudes is therefore essential for subsequent
130 analysis.

131

132 2.2 Shape and scaling of response functions

133

134 The response function used in the CSD process can be either simulated or derived
135 directly from the data. Following the latter approach, which is more common, voxels that have
136 a high chance of containing single fiber populations are used to calibrate the response function.
137 A straightforward approach to numerically implement the concept of a single fiber population
138 is to threshold, for instance, the fractional anisotropy (FA), above a pre-defined value.
139 However, the choice of FA threshold is not trivial and can cause inaccuracies in the response
140 function estimation [12]. A data-driven method using a recursive calibration framework was
141 proposed to estimate the response function from the subject data in an unbiased way [12].
142 This method estimates which voxels contain single fiber populations by iteratively excluding
143 voxels which do not have a single dominant orientation and updating the estimated response
144 function.

145 The choice of the fiber response function has an impact on the peak directions and
146 magnitudes of the FODs [10,15,19]. Theoretically, changes in the response function are
147 directly reflected in the FOD estimation, but should affect only peak magnitudes while leaving
148 their orientations untouched [6,10]. However, in practice, due to the low SNR level in diffusion-
149 weighted MRI data, the ill-posedness of inverse problems, and the regularization process, the
150 effects of the choice of response function on the FODs become less obvious.

151 Parker et al. [15] investigated alterations of response function by changing its FA value.
152 Here, we acknowledge that changing the FA affects both the scale and the shape of the
153 response function. It is thus not straightforward to disentangle an FOD change into scale and

154 shape effects. To this end, we decompose general changes in the response function into
 155 specific changes in shape and scale [8] and analyze their individual effects on the FOD
 156 characteristics (i.e., magnitude, the number of peaks, and peak orientations). The following
 157 sections describe how we can achieve such changes in shape and scale of the response
 158 functions in the simulated and in vivo diffusion MRI data experiments.

159

160 2.3 Simulation experiments

161

162 2.3.1 Modeling of single fiber populations and response functions

163

164 If the diffusivity D associated with the underlying fiber population is expressed by an
 165 axially symmetric diffusion tensor, whose first eigenvector is in parallel with the z-axis in the
 166 reference coordinate frame, then $D(\theta, \varphi)$ can be written as (Anderson 2005)

$$D_{(\theta, \varphi)} = \begin{bmatrix} \sin \theta \cos \varphi & \sin \theta \sin \varphi & \cos \theta \end{bmatrix} \begin{bmatrix} \beta & 0 & 0 \\ 0 & \beta & 0 \\ 0 & 0 & \lambda \end{bmatrix} \begin{bmatrix} \sin \theta \cos \varphi \\ \sin \theta \sin \varphi \\ \cos \theta \end{bmatrix}, \quad (1)$$

167 where λ and β are the axial and the radial diffusivity of the single fiber population, (θ, φ) is the
 168 polar angle set between the fiber orientation and the applied gradient. Given the axial
 169 symmetry property of the diffusion tensor, Eq. (1) can be simplified as

$$D_{(\theta)} = \lambda \cos^2 \theta + \beta \sin^2 \theta = \alpha \cos^2 \theta + \beta, \quad (2)$$

170 where $\alpha = \lambda - \beta$ is the absolute difference between the axial and radial diffusivity. For simplicity,
 171 if we assume that the signal $S(\theta, \varphi)$ from each fiber population is a function of $D(\theta, \varphi)$, then the
 172 diffusion-weighted signal S can then be rewritten as [3]

$$S_{(\theta, \varphi)} = S_0 e^{-bD_{(\theta, \varphi)}}, \quad (3)$$

173 where S_0 is the non-diffusion-weighted signal and b is the b-value that represents the strength
 174 of diffusion weighting. Combining Eq. (1) – Eq. (3), the diffusion-weighted signals can be
 175 expressed as [18]

$$S(\theta) = S_0 e^{-b(\alpha \cos^2 \theta + \beta)} = S_0 K e^{-b\alpha \cos^2 \theta}, \quad (4)$$

176 where $K = e^{-b\beta}$. Eq. (4) highlights the dependency of S on the shape factor α and the scaling
177 factor K , following the definition in previous studies [8]. In this equation, the scaling factor K
178 depends only on the radial diffusivity of the fiber response, representing the isotropic diffusion
179 within the fiber population, whereas the shape factor α depends on the difference between the
180 axial and radial diffusivities, representing the anisotropic diffusion within the fiber population.

181

182 2.3.2 Modifying the shape and scaling factor of the response functions

183

184 Since the response function R is intrinsically based on the shape and scaling of the
185 fiber population diffusivities, R can be written in the same form as the signal of a fiber population
186 imposed by the gradient at an elevation angle θ with the fiber orientation, which is identical to
187 Eq. (4), i.e.,

$$R(\theta) = S_0 K e^{-b\alpha \cos^2 \theta}. \quad (5)$$

188 According to Eq. (5), we can modify (i) the shape factor α of the response function, by varying
189 only the axial diffusivity with a fixed radial diffusivity, to keep K constant; and (ii) the scaling
190 factor K of the response function, by changing simultaneously the axial and radial diffusivity,
191 to not alter the shape factor α . We can then study the effects of R on FOD characteristics, by
192 selectively introducing a discrepancy into the shape or the scale of a simulated single fiber
193 signal with respect to the response function.

194

195 2.3.3 Modeling of multi-fiber populations

196

197 We model the diffusion-weighted signal within a voxel as the sum of multiple
198 compartments measured from each fiber population. Each compartment is assumed to share
199 an identical response function, so the diffusion-weighted signals are depending only on the
200 orientations of the fiber populations in the voxel and on data noise. We further assume that
201 there is no exchange of water molecules between fiber populations, and that each single fiber

202 population can be represented by a signal $S_{i(\theta)}$ (where i denotes the i^{th} fiber population). The
203 signal S_{DW} generated by a crossing fiber configuration can then be described by

$$S_{DW} = \sum_{i=1}^n f_i S_{i(\theta)}, \quad (6)$$

204 where f_i is the volume fraction of each fiber population, n is the total number of fiber
205 populations intercrossing the voxel, and $i(\theta)$ is the angle between the applied gradient and the
206 i^{th} fiber population. In our work, we focus on configurations of two crossing fiber populations,
207 but the equations of generating the diffusion-weighted signals can also be extended to analyze
208 the FOD characteristics for more than two fiber populations.

209

210 2.3.4 Data analysis

211

212 Amongst the SD frameworks, the CSD approach is implemented in several software
213 packages, such as *MRtrix* [25], *Dipy* [26] and *ExploreDTI* [27]. In this work, the FODs were
214 estimated with CSD as implemented in *ExploreDTI*. The FOD peak orientations, which are
215 assumed to reflect the underlying fiber orientations [6], and the magnitudes of the FOD peaks,
216 were extracted using a Newton-Raphson gradient descent method [28]. All FOD peaks that
217 were smaller than an absolute threshold of 0.1 were regarded as contributions from noise and
218 thus discarded to reduce false positives [29]. All peaks were clustered to the nearest simulated
219 peak directions, by using an angular threshold of 45° to determine whether or not two peaks
220 were belonging to the same fiber population. In case of simulating multiple fiber populations,
221 only the estimated FOD peaks closest to the simulated fiber populations were considered. For
222 each simulation, the mean and standard deviation of the following FOD metrics were
223 evaluated:

- 224 a. the average difference between the estimated and simulated number of FOD peaks;
- 225 b. the angular deviations between the estimated FOD peak orientation and the simulated fiber
226 orientation;
- 227 c. the estimated separation angles in case of multiple fiber populations;
- 228 d. the FOD peak magnitudes in case of single fiber populations;

229 e. the percentage difference of the estimated AFD with respect to the AFD with the reference
230 response function.

231 The AFD computation was performed as the integral of the FOD magnitudes assigned
232 to each peak, which in the literature is commonly referred to as “lobe”. The calculation of the
233 AFD is similar to what was used in a previous study [30], except that we use the gradients
234 generated by the electromagnetic model [31] to segment the FODs for each fiber population
235 instead of using gradients generated by an icosahedron model.

236

237 2.4 Parameter settings

238

239 We simulated different fiber configurations with a predefined b -value equal to 3000 s/
240 mm^2 , a set of 60 gradient directions [31], and $S_0 = 1$. Rician noise (1000 noise instances) was
241 added to the diffusion weighted signals to simulate SNR (with respect to S_0) levels of [50 40
242 30 20 15 10]. In the first simulation, a single-fiber configuration was generated with the main
243 diffusion direction along the z-axis, setting $\alpha = 1.2 \times 10^{-3} \text{ mm}^2/\text{s}$ and $K = 0.4$ (i.e. $\beta \sim (0.3 \times$
244 $10^{-3} \text{ mm}^2/\text{s})$). In the second simulation, a second fiber population was rotated around the y-
245 axis and combined with the single-fiber population generated in the first simulation to achieve
246 a separation angle ω . Here we simulated crossing fiber populations with separation angles ω
247 = [90°, 75°, 60°, 55°, 50°, 45°, 40°].

248 For both simulations, two sets of response functions were tested to achieve (a) different
249 shape but the same scaling factors, by increasing α from $0.6 \times 10^{-3} \text{ mm}^2/\text{s}$ to 1.8×10^{-3}
250 mm^2/s with steps of $0.1 \times 10^{-3} \text{ mm}^2/\text{s}$, while keeping K constant (Fig. 1a); and (b) the same
251 shape but different scaling factors, by decreasing K from 0.7 to 0.3 with steps of 0.1, while
252 keeping α constant (Fig. 1b).

253

254 **Fig. 1. The 2D projection of response functions obtained by changing (a) the shape**
255 **factor α and (b) the scaling factor K .** The shape factors are defined from $0.6 \times 10^{-3} \text{ mm}^2/\text{s}$

256 to $1.8 \times 10^{-3} \text{ mm}^2/\text{s}$ in steps of $0.1 \times 10^{-3} \text{ mm}^2/\text{s}$. The scaling factors are varied from 0.7 to
257 0.3 in steps of 0.05.

258

259 2.5 Peak clustering and angular threshold

260

261 We clustered the peak directions to make sure that we are always comparing the
262 angular deviations between the simulated fiber orientation and the FOD peak orientation most
263 closely aligned to that orientation. Like in other studies [16,32,33] that compare axial and radial
264 diffusion characteristics, we also included an angular threshold (e.g., $\cos(\theta) > 0.7$, which
265 means approximately $\theta < 45^\circ$) to make sure the correct peaks were being extracted for further
266 evaluations.

267

268 2.6 In vivo data experiments

269

270 Diffusion-weighted MRI data of a single HCP subject was further used to illustrate the
271 effects of ill-defined response functions on voxel-wise FOD characteristics and brain
272 tractography. In summary, diffusion-weighted images were acquired along 90 diffusion
273 gradient directions with a b -value of $3000 \text{ s}/\text{mm}^2$ in addition to 18 non-diffusion-weighted
274 images, and with an isotropic spatial resolution of $1.25 \times 1.25 \times 1.25 \text{ mm}^3$. We performed CSD
275 based tractography in *ExploreDTI* with a step size of 1 mm, an FOD threshold of 0.1, an
276 angular threshold of 30° , and seeding points per $2\text{mm} \times 2\text{mm} \times 2\text{mm}$ across the whole brain.
277 All the tracts were constructed with deterministic fiber tracking to facilitate data interpretation.

278

279 2.6.1 Modeling the response function

280

281 The reference response function for the in vivo dataset was represented by the diffusion
282 tensor fit to the response function, as estimated with the recursive calibration approach [12].
283 Similar to the method described in Section 2.3.2, the diffusion tensor was used to model the
284 changes in the shape and the scaling factor of the response functions. The shape factor α of

285 the response function was modified by +/- $[0.1 - 0.3 \times 10^{-3} \text{ mm}^2/\text{s}]$, while the scaling factor K
286 was modified by +/- $[0.1 - 0.2]$.

287

288 2.6.2 Evaluation of in-vivo data

289

290 In analogy with the simulations, we computed the voxel-wise difference in number of
291 estimated FOD peaks, the angular deviations of the main orientation, and the percentage
292 difference in AFD of the dominant fiber orientation, for all the estimated FODs. The
293 comparisons of number of FOD peaks were computed for the whole brain, whereas the
294 comparisons of angular deviation and AFD were only computed for voxels with $FA > 0.2$.

295 Individual white matter fiber bundles were extracted by using the regions of interest
296 (ROIs) as suggested by Wakana [34]. The segmented fiber pathways include parts of the
297 splenium of corpus callosum (sCC), the genu of corpus callosum (gCC), the cingulum (Cg),
298 the uncinate fasciculus (UF), the corticospinal tract (CST), and the temporal part of the superior
299 longitudinal fasciculus (tSLF). The average FOD characteristics for each fiber bundle were
300 calculated. In addition, FOD characteristics of the response function were computed from (1)
301 the region with a single fiber population as identified during the recursive calibration step
302 (referred to as “SFP-mask”); and (2) the region with voxels for which $FA > 0.2$ (referred to as
303 “FA-mask”).

304 3. Results

305

306 3.1 FOD characteristics of single fiber populations

307

308 Fig. 2 shows the effect of changing the shape factor and the scaling factor of the
309 response function on the FOD characteristics in a single fiber population. At $SNR < 20$, the
310 average number of spurious peaks increases when the shape factor increases, but only slightly
311 increases when the scaling factor decreases (Fig. 2A). The angular deviation depends mainly
312 on the SNR and is far less affected by changes in shape or scale factor of the response function

313 (Fig. 2B). By contrast, changes in peak magnitude (Fig. 2C) and the AFD (Fig. 2D) as a function
314 of shape and scaling factor of the response function are more pronounced than due to
315 differences in SNR level alone. Notice that the effect of changing the scaling factor (up to
316 ~60%) is roughly three times larger compared to changing the shape factor (up to ~20%).

317

318 **Fig. 2. Effect of simulating changes in the response function on FOD characteristics for**
319 **a single fiber configuration at different SNR levels.** Shape factor α and the scaling factor
320 K of the response function (RF) are varied at different SNR levels to investigate (A) the
321 introduction of spurious peaks, i.e., the average difference between the estimated and
322 predefined number of FOD peaks; (B) the confidence interval (average \pm standard error) of the
323 angular deviation of the primary FOD peak; (C) the percentage difference between the
324 amplitudes of the estimated FOD peak and the ground-truth FOD peak; and (D) the percentage
325 difference between the estimated AFD of the primary fiber population and the ground-truth
326 AFD. The dashed vertical lines represent the ground-truth values.

327

328 3.2 Occurrence of spurious peaks

329

330 Fig. 3 shows the average difference between the number of estimated and simulated
331 FOD peaks in relation to the shape (left) and the scaling (right) factor of the response functions
332 for different SNR levels. Overall, performing spherical deconvolution with sharper response
333 functions (i.e., higher values of the shape factor) generally introduces more spurious peaks.
334 On the other hand, CSD fails to extract all the simulated peaks from the estimated FODs when
335 the response function shape factor has smaller values, in particular for separation angles
336 below 55° . With higher noise levels, more spurious peaks are introduced, especially for higher
337 values of the shape factor. Furthermore, adjusting the scaling factor has no significant effect
338 on the estimated number of spurious peaks. While there are hardly any spurious peaks
339 introduced at the lower noise levels (SNR = 30 and 50), additional incorrect peaks can be
340 observed at the higher noise level (SNR = 10).

341

342 **Fig. 3. The average difference between the number of estimated and simulated FOD**
343 **peaks as a function of shape (left) and scaling (right) factor of the response function**
344 **(RF) at three SNR levels (different SNR for each row).** Brighter yellow areas show a higher
345 probability of introducing spurious peaks, whereas darker blue areas show a higher probability
346 of merging the two simulated peaks into one peak. The dashed vertical lines indicate that the
347 settings of the response function are identical to those used for generating the underlying
348 signals. Notice that different scaling of the colorbars were used for better contrast.

349

350 3.3 Angular deviation

351

352 3.3.1 The effect of the shape factor

353

354 Fig. 4 shows the results of investigating the effect of the response function's shape
355 factor on the angular characteristics of FOD peaks at SNR = 50, 30 and 10 for crossing fiber
356 configurations with different separation angles. At lower noise levels (SNR = 30 and 50), lower
357 values of the shape factor generally cause an underestimation of the separation angles, except
358 when the two simulated fiber populations are orthogonal to each other (i.e., 90°) (Fig. 4A). At
359 the higher noise level (i.e., SNR = 10), the bias in the estimated separation angle due to
360 changes in the shape factor is swamped by the noise itself, especially for lower separation
361 angles. From the observed angular deviations in Fig. 4B (the first peak) and Fig. 4C (the
362 second peak) we can observe, in general, that for smaller simulated separation angles, the
363 adverse effects of changing the shape factor of the response function on the estimated FOD
364 angular characteristics are more pronounced.

365

366 **Fig. 4. Results of exploring the impact of response functions with different shape factor**
367 **α on the FOD peaks for crossing fiber configurations simulated with separation angles**
368 **ranging from 90° to 40°.** Fig. 4A shows the estimated separation angles between the two

369 primary peaks. Dashed horizontal lines indicate the simulated separation angles. Fig. 4B and
370 Fig. 4C show the angular deviations between the estimated first (p_1) and second (p_2) FOD
371 peaks and their corresponding simulated fiber orientations. Solid line interruptions occurred
372 when one of the two peaks was not detected. The means of the estimated values are plotted
373 with the standard error as the shaded areas. Dashed vertical lines are defined as in Fig. 3.

374

375 3.3.2 The effect of the scaling factor

376

377 Fig. 5 shows the angular deviations between the orientation of the estimated FOD
378 peaks and the simulated fiber orientations as a function of the scaling factor. Overall, crossing
379 fibers with separation angles smaller than 45° show larger angular deviations than those with
380 more orthogonal separation angles. In Fig. 5A, the estimated separation angles do not change
381 significantly as a function of the scaling factor of the response function. Nevertheless, smaller
382 simulated separation angles result in a larger bias of the estimated separation angles. Fig. 5B
383 and Fig. 5C present the angular deviations of the first and second FOD peak, respectively. The
384 angular deviations are not significantly affected by the scaling factor, but do depend on the
385 magnitude of the separation angles of the two fiber populations.

386

387 **Fig. 5. The effect of varying the scaling factor (K) of the response function on the FOD**
388 **peaks for crossing fiber configurations simulated with separation angles ranging from**
389 **90° to 40° .** Fig. 5A shows the estimated separation angles between the two primary peaks.
390 Dashed horizontal lines indicate the simulated separation angles. Fig. 5B and Fig. 5C show
391 the angular deviations between the estimated first (p_1) and second (p_2) FOD peaks and the
392 corresponding simulated fiber orientations. Solid line interruptions occurred when one of the
393 two peaks was not detected. The means of the estimated values are plotted with the standard
394 error as the shaded areas. Dashed vertical lines are defined as in Fig. 3.

395

396 3.4 AFD per fixel

397

398 Fig. 6 shows the percentage difference of the AFD of the first and second fiber
399 population in relation to the response function shape factor (A, B) and scaling factor (C, D). In
400 Fig. 6A, at SNR 50 and 30, the AFD started at a very high value when the shape factor is
401 smaller than 0.8, 1.0 and 1.4×10^{-3} mm²/s for the simulated separation angles of 55°, 50° and
402 45°, respectively. The AFD values converge to the AFD of the other separation angles as the
403 shape factor increases. As shown in the angular characteristics results (Fig. 4), when the
404 response function becomes sharper, the drop points of AFD for small separation angles
405 indicate the boundaries at which CSD is just able to separate the two fiber populations. In case
406 of the 40° separation angle, only one FOD peak is obtained. The large difference in AFD for
407 small separation angles (45°-55°) with decreased shape factors can be a confounding factor in
408 inter-subject comparisons of AFD studies, which will be discussed further in Section 4.3. At
409 SNR 10, the AFD differences are more related to noise than to the shape of the response
410 function for smaller separation angles (below 60°). As for the second peak (Fig. 6B), the AFD
411 can change from -30% to 20% when the shape factor was modified from -50% to 50%,
412 respectively.

413

414 **Fig. 6. The percentage difference of the estimated AFD of the first peak (p1) and the**
415 **second peak (p2) in relation to the response function shape factor α (A, B) and scaling**
416 **factor K (C, D) at different SNR levels.** The quick drop of the AFD difference while increasing
417 the shape factor indicates when CSD was able to separate the two fiber populations. Dashed
418 vertical lines are defined as in Fig. 3.

419 Fig. 6C and Fig. 6D show the percentage difference of the AFD of the first and second
420 fiber population in relation to the scaling factor of the response function. In line with the
421 simulation results for single fiber populations (Fig. 2D), AFD can change up to 80% due to the
422 scaling factor changes for the second peak. For simulated separation angles of approximately
423 45°, AFD of the first fiber population can be over-estimated up to as much as 150%. For the

424 other simulated separation angles, the AFD of the primary peak can vary from -40% to 70% at
425 SNR = 50 and SNR = 30, irrespective of the simulated separation angles. Notice that the AFD
426 changes are not linearly related with changes in the scaling factor.

427

428 3.5 In vivo HCP data set

429

430 3.5.1 FOD characteristics of white matter

431

432 In this section, we present the effect of changing the shape and scaling factors of the
433 response function on FOD characteristics for an axial slice of the HCP data set. The difference
434 in number of FOD peaks per voxel is shown in Fig. 7. Differences are typically seen in areas
435 with partial volume effects and with mostly a peak number difference value of one. When the
436 difference in shape factor, denoted by $\Delta\alpha$, increases by $0.1 \times 10^{-3} \text{ mm}^2/\text{s}$ to 0.3×10^{-3}
437 mm^2/s , one can see the increase in occurrence of peak number deviations, such as, for
438 instance, in mid-sagittal regions of the corpus callosum. With the increase of difference in
439 scaling factor, denoted by ΔK , regions containing CSF showed higher peak number differences
440 than regions with white and gray matter.

441

442 **Fig. 7. The difference between the number of FOD peaks estimated with the tensor-**
443 **based response function and the number of FOD peaks computed with the response**
444 **function modified according to certain changes in scaling (ΔK) and shape ($\Delta\alpha$) factors.**

445 The background is an axial view of the FA map. The peak number difference mostly occurs in
446 grey matter and CSF areas, and crossing fiber regions for white matter, as indicated by the
447 colormap. In regions with single fiber populations (e.g., middle parts of the corpus callosum)
448 spurious peaks are hardly present.

449

450 Fig. 8 shows the angular difference between the primary FOD peak, computed with the
451 tensor-fit to the recursive calibrated response function, and the FOD peak obtained with the

452 modified shape and scale factors of the response function. In general, regions containing
453 crossing fibers are affected most when modifying the shape of response functions, with angular
454 deviations of the main FOD peak of up to 3° . Notice that the angular deviation is mostly affected
455 by changing the shape factor, rather than the scaling factor. In addition, while changing ΔK did
456 not affect the angular deviation, increasing the magnitude of $\Delta\alpha$ resulted in larger angular
457 deviations in the same locations.

458

459 **Fig. 8. The angular deviations between the FOD peaks estimated with the tensor-fit of**
460 **the response function and the FOD peaks estimated with the response function**
461 **modified according to certain changes in scaling (ΔK) and shape ($\Delta\alpha$) factors.** The
462 background is an axial view of the FA map and, for clarity, the angular deviations are shown
463 only in regions where $FA > 0.2$. Most angular differences are in the range of $0-3^\circ$. Similar to the
464 results of spurious peaks shown in Fig. 7, angular deviations are larger in regions with crossing
465 fiber populations than regions with single fiber populations, such as the middle part of the
466 corpus callosum. Notice that the angular deviations are much higher with regard to shape
467 factor changes than scaling factor changes.

468

469 Fig. 9 shows the voxel-wise AFD difference for the dominant fiber direction between
470 the FOD estimated using the tensor-fit to the recursive calibrated response function and the
471 FOD obtained with the modified shape and scale factors of the response function for the HCP
472 data set. The AFD shows a very different pattern in relation to the shape factor changes
473 compared to scaling factor changes. The AFD differences are homogenous throughout the
474 brain when the scaling factor varies, while the outliers indicate the voxels where there are
475 potential geometrical differences in the estimated AFD from the reference, such as merging or
476 spurious peaks. The AFD differences are up to 98% when the scaling factor K decreased by
477 0.2. When changing the shape factor with $-0.3 \times 10^{-3} \text{ mm}^2/\text{s}$ to $0.3 \times 10^{-3} \text{ mm}^2/\text{s}$, the highest
478 differences (around 6 to 8%) were observed in areas with a single-fiber population, such as

479 the corpus callosum. Notice that bigger changes of the shape factor α makes the AFD
480 difference more heterogeneous across the brain.

481

482 **Fig. 9. The percentage difference of the apparent fiber density (AFD) between the FOD**
483 **peaks estimated with the tensor-fit of the response function and the FOD peaks**
484 **estimated with the response function modified according to certain changes in scaling**
485 **(ΔK) and shape ($\Delta\alpha$) factors.** The background is an axial view of the FA map and, for clarity,
486 the AFD percentage differences are shown only in regions where FA > 0.2. Notice that the
487 AFD difference stays homogenous with respect to the scaling factor changes, whereas it is
488 heterogeneous when the shape factor changes.

489

490 3.5.2 Effect on fiber tractography

491

492 Fig. 10 shows the effect of changing the scaling and shape factors of the response
493 function on the reconstruction of the pathways of the tSLF. The reference trajectories (shown
494 in yellow) are computed with the recursive calibration method. While not much differences can
495 be observed for the main part of the reconstructed tracts, changing the response function
496 mainly affected the trajectories where the tSLF enters the frontal and temporal lobes (see
497 enlarged regions in Fig. 10).

498

499 **Fig. 10. The temporal part of the superior longitudinal fasciculus (tSLF) reconstructed**
500 **with the FODs estimated using the tensor-fit to the recursively calibrated response**
501 **function (yellow), and the tSLF from the same ROIs reconstructed with FODs estimated**
502 **using the modified response functions.** The other fiber bundles (shown in red, blue, cyan,
503 magenta, and green) indicate the effect of changing the scaling (ΔK) and shape ($\Delta\alpha$) factors
504 of the response function on the trajectory of the tSLF. Notice the subtle differences in how the
505 fiber trajectories terminate in the temporal lobe (zoomed areas; the “+” and “-” indicate increase
506 and decrease in the scaling and shape factors, respectively).

507

508 Fig. 11 shows the FOD characteristics for the FA-mask, the SFP-mask, and the
509 extracted fiber bundles (gCC, sCC, CST, UF, Cg and tSLF). From all the three FOD
510 characteristics (i.e., spurious peaks, angular deviations, and AFD percentage differences), we
511 can spot a similar trend for all the bundles and the masks with respect to the changes in the
512 shape and scaling factors of the response function. Overall, the UF has the highest average
513 number of spurious peaks. The lowest average angular deviations of the first FOD peak can
514 be seen for the SFP-mask. Furthermore, the alterations of the shape factor of the response
515 function can cause angular deviations up to 6° , while the alterations of the scaling factor hardly
516 cause any angular differences in the masks or the selected fiber bundles (see the enlarged
517 plot). Finally, the differences in AFD are relatively homogenous across the extracted fiber
518 bundles and masks with as a function of changing the shape or the scaling factors.

519

520 **Fig. 11. The average number of spurious peaks, the average angular deviations, and the**
521 **average percentage differences in AFD of the first fiber population for the FA-mask, the**
522 **SFP-mask, and the selected fiber bundles (shown on the right) when a modified**
523 **response function was used in comparison to the original tensor-fit to the recursive**
524 **calibrated response function.** The effect of the changes in the scaling (ΔK) and shape ($\Delta\alpha$)
525 factors of the response function on the selected fiber bundles are reflected in the different color
526 encoding. sCC = splenium of corpus callosum; gCC = genu of corpus callosum; Cg = cingulum;
527 UF = uncinata fasciculus; CST = corticospinal tract; tSLF = temporal part of superior
528 longitudinal fasciculus.

529 4. Discussion

530

531 In this work we investigated the effect of changing response function properties on the
532 FOD characteristics using numerical simulations and in vivo HCP data. In particular, we show
533 how miscalibration of the response function, as defined by adjusting the scaling and shape

534 factors, can introduce a bias in the orientation and magnitude of fiber population peaks. Our
535 findings demonstrate that CSD is prone to produce spurious FOD peaks in the presence of
536 miscalibrated response functions, especially in data with insufficient SNR levels. The
537 occurrence of such spurious peaks can also introduce inaccurate fiber pathway
538 reconstructions with fiber tractography. Overall, in agreement with former studies, spurious
539 peaks are introduced due to overestimating the shape factor of the response function, while
540 underestimating the shape factor will result in lower angular resolution of the FOD lobes
541 [10,15]. Proper tuning of the response function is therefore necessary to achieve an optimal
542 balance between increasing the angular resolution and minimizing the number of spurious
543 peaks, especially for smaller separation angles (i.e., below 60°) and at low SNR levels. Further,
544 AFD estimation can be influenced by the choice of response function, which will be discussed
545 in section 4.3.

546

547 4.1 Effect of shape and scaling factors with simulations

548

549 At SNR levels of 30 and 50, the FOD characteristics are consistently affected by the
550 choice of the response functions, while at SNR of 10, noise is the dominating factor that affects
551 the FOD properties (Fig. 3). In addition, more spurious peaks are observed at SNR of 10. At
552 relatively high SNR levels, the shape factor of the response function has a greater impact on
553 the results than the scaling factor. In particular, using a sharper response function for
554 separation angles below 50° can potentially increase the angular resolution of CSD and can,
555 therefore, improve the estimation of the number of peaks (Fig. 3). The shape of the response
556 function was reported to vary with axonal injury and brain maturation, whereas the scaling
557 factor was observed to change as result of demyelination, axonal diameters and axonal density
558 changes [10,35]. This implies that in brain regions affected by disease, applying CSD with a
559 response function determined by healthy white matter data can result in unreliable estimates
560 of FOD characteristics.

561

562 4.2 Effect of the separation angle between crossing fiber populations

563

564 The extent to which the FODs will be affected by the response function depends largely
565 on the separation angle between crossing fiber populations (Fig. 4). More orthogonally
566 crossing fiber orientations are less sensitive to response function changes, as originally
567 suggested in the spherical deconvolution paper [6]. In voxels containing crossing fiber
568 configurations with smaller separation angles (e.g., below 60°), the average angular deviations
569 and their variance increase rapidly with lower shape factors of the response function. By
570 contrast, a higher shape factor of the response function results in a smaller bias in the
571 computation of the FOD peak orientations than the underestimation of the shape factor (Fig. 4
572 and Fig. 5).

573

574 4.3 Effect of shape factor on AFD

575

576 For fiber populations with separation angles below 55° , CSD fails to estimate the correct
577 number of peaks when response functions with a lower shape factor are employed, leading to
578 artificially higher AFD values (Fig. 6). As FOD peaks merge together when the shape factor is
579 further decreased, the AFD becomes close to the integral of the total FOD amplitudes within
580 the voxel. This is shown in Fig. 6 for simulated separation angles between 45° to 55° . For these
581 relatively small separation angles, the large AFD difference is caused by the limited angular
582 resolution of CSD with the simulated settings. Previous studies [36] reports AFD as a more
583 sensitive diffusion marker in traumatic brain injury than the traditional metrics. However, one
584 should be aware that these changes in AFD in the presence of pathology could result from
585 global response function differences between subjects, rather than local diffusivities
586 alterations.

587

588 4.4 Effect of FOD angular deviations on fiber tracking

589

590 If the angular deviations of the FOD peaks are similar in the neighborhood voxels along
591 the white matter pathways, accumulating effects on reconstructed fibers will be significant. By
592 contrast, the heterogenous angular deviations of the FOD peaks may only change the voxel-
593 wise characteristics like AFD and number of fiber population peaks, the fiber pathways remains
594 if the angular deviations of FOD was not big enough to end in different voxels in the trajectory.
595 Generally, fiber tractography results will not be severely affected in the main part of the fiber
596 bundles, but may show subtle differences at the edges (Fig. 10). In addition, the termination of
597 fiber pathways passing through crossing regions can be affected [12]. With the in vivo HCP
598 data, only minor changes in the tSLF trajectories are detected when using the modified
599 response functions with different shape factors. Nevertheless, an inaccurate response function
600 will influence the FODs and subsequently fiber tractography results.

601

602 4.5 Limitations and future directions

603

604 The reference value of the shape and scaling factor of the simulated diffusion-weighted
605 signals match with the values in the corpus callosum as reported before. However, recent
606 studies [37–40] indicated that the diffusivities of fiber bundles in the brain are not always the
607 same. There is not a full map of diffusivity characteristics of each white matter structure yet.
608 Although our simulation study included the same configurations of crossing fiber bundles in a
609 voxel, in reality, the diffusivities of these crossing fibers may not be identical.

610 In this study, we showed tractography results of an HCP subject using the tensor-fit to
611 the recursively calibrated response function and modified response functions. In group studies
612 between healthy subjects and patients with neural degradation diseases (e.g., Alzheimer's
613 disease), it would be useful to compare the alterations of response functions. If there is a
614 group-wise alteration of the shape and the scaling factor of the response functions, we should
615 first exclude the deviations of the diffusivities of the diseased group from the healthy subjects,
616 to ensure that FOD characteristics and fiber tractography changes are not the effects of the

617 response function alteration itself. Furthermore, we can separate the effects of disease on
618 white matter fiber tracking from the effects of response functions used in the FOD estimation.

619 **5. Conclusion**

620

621 This study demonstrates with numerical simulations and in vivo HCP data that
622 decreasing the shape factor of the response function can cause large angular deviations of the
623 FOD peak orientations in crossing fibers. Sharper response functions are responsible for
624 introducing spurious peaks, which can also confound subsequent tractography results.
625 Extremely low shape factors of the response function can cause significant angular deviations
626 and may complicate the interpretation in studies involving pathology. In addition, although
627 individual angular deviations of FOD peak orientations are small for single voxels at most
628 separation angles, the adverse effect can accumulate for brain tractography. Since smaller
629 separation angles are more sensitive to changes of response function shape factors, future
630 work of inter-subject AFD and pathological groups should be aware of this possible
631 confounding factor when investigating brain structures with crossing fiber configurations.

632

633

634 References

635

- 636 1. Stejskal EO, Tanner JE. Spin diffusion measurements: Spin echoes in the presence of a time-
637 dependent field gradient. *J Chem Phys*. 1965;42(1):288–92.
- 638 2. Le Bihan D, Breton E, Lallemand D, Grenier P, Cabanis E, Laval-Jeantet M. MR imaging of
639 intravoxel incoherent motions: application to diffusion and perfusion in neurologic disorders.
640 *Radiology*. 1986;161:401–7.
- 641 3. Basser PJ, Mattiello J, LeBihan D. MR diffusion tensor spectroscopy and imaging. *Biophys J*
642 [Internet]. 1994;66(1):259–67. Available from: [http://dx.doi.org/10.1016/S0006-](http://dx.doi.org/10.1016/S0006-3495(94)80775-1)
643 [3495\(94\)80775-1](http://dx.doi.org/10.1016/S0006-3495(94)80775-1)
- 644 4. Jeurissen B, Leemans A, Tournier JD, Jones DK, Sijbers J. Investigating the prevalence of
645 complex fiber configurations in white matter tissue with diffusion magnetic resonance
646 imaging. *Hum Brain Mapp*. 2013;34(11):2747–66.
- 647 5. Behrens TEJ, Berg HJ, Jbabdi S, Rushworth MFS, Woolrich MW. Probabilistic diffusion
648 tractography with multiple fibre orientations: What can we gain? *Neuroimage*. 2007;34:144–
649 55.
- 650 6. Tournier JD, Calamante F, Gadian DG, Connelly A. Direct estimation of the fiber orientation
651 density function from diffusion-weighted MRI data using spherical deconvolution.
652 *Neuroimage*. 2004;23(3):1176–85.
- 653 7. Tournier JD, Calamante F, Connelly A. Robust determination of the fibre orientation
654 distribution in diffusion MRI: Non-negativity constrained super-resolved spherical
655 deconvolution. *Neuroimage*. 2007;35:1459–72.
- 656 8. Dell’Acqua F, Rizzo G, Scifo P, Clarke RA, Scotti G, Fazio F. A model-based deconvolution
657 approach to solve fiber crossing in diffusion-weighted MR imaging. *IEEE Trans Biomed Eng*.
658 2007;54(3):462–72.
- 659 9. Raffelt D, Tournier JD, Rose S, Ridgway GR, Henderson R, Crozier S, et al. Apparent Fibre
660 Density: A novel measure for the analysis of diffusion-weighted magnetic resonance images.
661 *Neuroimage* [Internet]. 2012;59(4):3976–94. Available from:
662 <http://dx.doi.org/10.1016/j.neuroimage.2011.10.045>
- 663 10. Dell’Acqua F, Simmons A, Williams SCR, Catani M. Can spherical deconvolution provide more
664 information than fiber orientations? Hindrance modulated orientational anisotropy, a true-
665 tract specific index to characterize white matter diffusion. *Hum Brain Mapp*.
666 2013;34(10):2464–83.
- 667 11. Dhollander T, Raffelt D, Connelly A. Unsupervised 3-tissue response function estimation from
668 single-shell or multi-shell diffusion MR data without a co-registered T1 image. *ISMRM Work*
669 *Break Barriers Diffus MRI* [Internet]. 2016;5. Available from:
670 [https://www.researchgate.net/publication/307863133_Unsupervised_3-](https://www.researchgate.net/publication/307863133_Unsupervised_3-tissue_response_function_estimation_from_single-shell_or_multi-shell_diffusion_MR_data_without_a_co-registered_T1_image)
671 [tissue_response_function_estimation_from_single-shell_or_multi-](https://www.researchgate.net/publication/307863133_Unsupervised_3-tissue_response_function_estimation_from_single-shell_or_multi-shell_diffusion_MR_data_without_a_co-registered_T1_image)
672 [shell_diffusion_MR_data_without_a_co-registered_T1_image](https://www.researchgate.net/publication/307863133_Unsupervised_3-tissue_response_function_estimation_from_single-shell_or_multi-shell_diffusion_MR_data_without_a_co-registered_T1_image)
- 673 12. Tax CMW, Jeurissen B, Vos SB, Viergever M a., Leemans A. Recursive calibration of the fiber
674 response function for spherical deconvolution of diffusion MRI data. *Neuroimage* [Internet].
675 2014;86:67–80. Available from: <http://dx.doi.org/10.1016/j.neuroimage.2013.07.067>
- 676 13. Jeurissen B, Sijbers J, Tournier J-D. Assessing inter-subject variability of white matter response
677 functions used for constrained spherical deconvolution. In: *ISMRM 23th Annual Meeting*,

- 678 Toronto, Ontario, Canada. 2015. p. 2834.
- 679 14. Van Essen DC, Ugurbil K, Auerbach E, Barch D, Behrens TEJ, Bucholz R, et al. The Human
680 Connectome Project: A data acquisition perspective. *Neuroimage*. 2012;62(4):2222–31.
- 681 15. Parker GD, Marshall D, Rosin PL, Drage N, Richmond S, Jones DK. A pitfall in the reconstruction
682 of fibre ODFs using spherical deconvolution of diffusion MRI data. *Neuroimage* [Internet].
683 2013;65:433–48. Available from: <http://dx.doi.org/10.1016/j.neuroimage.2012.10.022>
- 684 16. Wheeler-Kingshott CAM, Cercignani M. About “axial” and “radial” diffusivities. *Magn Reson*
685 *Med*. 2009;61(5):1255–60.
- 686 17. Dell’Acqua F, Scifo P, Rizzo G, Catani M, Simmons A, Scotti G, et al. A modified damped
687 Richardson-Lucy algorithm to reduce isotropic background effects in spherical deconvolution.
688 *Neuroimage* [Internet]. 2010;49(2):1446–58. Available from:
689 <http://dx.doi.org/10.1016/j.neuroimage.2009.09.033>
- 690 18. Anderson AW. Measurement of fiber orientation distributions using high angular resolution
691 diffusion imaging. *Magn Reson Med*. 2005;54:1194–206.
- 692 19. Jian B, Vemuri BC. A unified computational framework for deconvolution to reconstruct
693 multiple fibers from diffusion weighted MRI. *IEEE Trans Med Imaging*. 2007;26(11):1464–71.
- 694 20. Descoteaux M, Angelino E, Fitzgibbons S, Deriche R. Regularized, fast, and robust analytical Q-
695 ball imaging. *Magn Reson Med*. 2007;58:497–510.
- 696 21. Tuch DS. Q-ball imaging. *Magn Reson Med*. 2004;52(6):1358–72.
- 697 22. Jansons KM, Alexander DC. Persistent angular structure: new insights from diffusion magnetic
698 resonance imaging data. *Inverse Probl* [Internet]. 2003;19(5):1031. Available from:
699 <http://stacks.iop.org/0266-5611/19/i=5/a=303>
- 700 23. Wedeen VJ, Hagmann P, Tseng WYI, Reese TG, Weisskoff RM. Mapping complex tissue
701 architecture with diffusion spectrum magnetic resonance imaging. *Magn Reson Med*.
702 2005;54(6):1377–86.
- 703 24. Ramirez-Manzanares A, Rivera M, Vemuri BC, Carney P, Mareei T. Diffusion basis functions
704 decomposition for estimating white matter intravoxel fiber geometry. *IEEE Trans Med*
705 *Imaging*. 2007;26(8):1091–102.
- 706 25. Tournier J-D, Calamante F, Connelly A. MRtrix: Diffusion tractography in crossing fiber regions.
707 *Int J Imaging Syst Technol* [Internet]. 2012;22(1):53–66. Available from:
708 <http://dx.doi.org/10.1002/ima.22005>
- 709 26. Garyfallidis E, Brett M, Amirbekian B, Rokem A, Van Der Walt S, Descoteaux M, et al. Dipy, a
710 library for the analysis of diffusion MRI data. *Front Neuroinform*. 2014;8:8.
- 711 27. Leemans A, Jeurissen B, Sijbers J, Jones D. ExploreDTI: a graphical toolbox for processing,
712 analyzing, and visualizing diffusion MR data. *Proc 17th Sci Meet Int Soc Magn Reson Med*
713 [Internet]. 2009;17(2):3537. Available from: [http://www.mendeley.com/research/exploredti-](http://www.mendeley.com/research/exploredti-a-graphical-toolbox-for-processing-analyzing-and-visualizing-diffusion-mr-data/%5Cnhttp://www.exploredti.com/ref/ExploreDTI_ISMRM_2009.pdf)
714 [a-graphical-toolbox-for-processing-analyzing-and-visualizing-diffusion-mr-](http://www.exploredti.com/ref/ExploreDTI_ISMRM_2009.pdf)
715 [data/%5Cnhttp://www.exploredti.com/ref/ExploreDTI_ISMRM_2009.pdf](http://www.exploredti.com/ref/ExploreDTI_ISMRM_2009.pdf)
- 716 28. Jeurissen B, Leemans A, Jones DK, Tournier J-D, Sijbers J. Probabilistic fiber tracking using the
717 residual bootstrap with constrained spherical deconvolution. *Hum Brain Mapp*. 2011
718 Mar;32(3):461–79.
- 719 29. Jeurissen B, Leemans A, Tournier J-D, Jones DK, Sijbers J. Investigating the prevalence of

- 720 complex fiber configurations in white matter tissue with diffusion magnetic resonance
721 imaging. *Hum Brain Mapp.* 2013;34(11):2747–66.
- 722 30. Smith RE, Tournier JD, Calamante F, Connelly A. SIFT: Spherical-deconvolution informed
723 filtering of tractograms. *Neuroimage [Internet]*. 2013;67:298–312. Available from:
724 <http://dx.doi.org/10.1016/j.neuroimage.2012.11.049>
- 725 31. Jones DK, Horsfield MA, Simmons A. Optimal strategies for measuring diffusion in anisotropic
726 systems by magnetic resonance imaging. *Magn Reson Med.* 1999;42(3):515–25.
- 727 32. Jbabdi S, Behrens TEJ, Smith SM. Crossing fibres in tract-based spatial statistics. *Neuroimage*
728 *[Internet]*. 2010;49(1):249–56. Available from:
729 <http://dx.doi.org/10.1016/j.neuroimage.2009.08.039>
- 730 33. Tax CMW, Westin CF, Dela Haije T, Fuster A, Viergever MA, Calabrese E, et al. Quantifying the
731 brain's sheet structure with normalized convolution. *Med Image Anal [Internet]*.
732 2017;39:162–77. Available from: <http://dx.doi.org/10.1016/j.media.2017.03.007>
- 733 34. Wakana S, Caprihan A, Panzenboeck MM, Fallon JH, Perry M, Gollub RL, et al. Reproducibility
734 of quantitative tractography methods applied to cerebral white matter. *Neuroimage*
735 *[Internet]*. 2007;36(3):630–44. Available from:
736 <http://dx.doi.org/10.1016/j.neuroimage.2007.02.049>
- 737 35. Feldman HM, Yeatman JD, Lee ES, Barde LHF, Gaman-Bean S. Diffusion tensor imaging: a
738 review for pediatric researchers and clinicians. *J Dev Behav Pediatr JDBP.* 2010;31(4):346.
- 739 36. Wright DK, Johnston LA, Kershaw J, Ordidge R, O'Brien TJ, Shultz SR. Changes in apparent fiber
740 density and track-weighted imaging metrics in white matter following experimental traumatic
741 brain injury. *J Neurotrauma.* 2017;34(13):2109–18.
- 742 37. Tax CMW, Novikov DS, Garyfallidis E, Viergever MA, Descoteaux M, Leemans A. Localizing and
743 Characterizing Single Fiber Populations Throughout the Brain. *Proc 23rd Annu Meet ISMRM,*
744 *Toronto, Canada [Internet]*. 2015;59(6):473. Available from:
745 <http://scil.dinf.usherbrooke.ca/wp-content/papers/tax-et-al-ismrm15a.pdf> VN -
746 readcube.com
- 747 38. Novikov DS, Jespersen SN, Kiselev VG, Fieremans E. Quantifying brain microstructure with
748 diffusion MRI: Theory and parameter estimation. *ArxivOrg [Internet]*. 2016;1–38. Available
749 from: <http://arxiv.org/abs/1612.02059>
- 750 39. Jespersen SN, Kroenke CD, Østergaard L, Ackerman JJH, Yablonskiy DA. Modeling dendrite
751 density from magnetic resonance diffusion measurements. *Neuroimage.* 2007;34(4):1473–86.
- 752 40. Kroenke CD, Ackerman JJH, Yablonskiy DA. On the nature of the NAA diffusion attenuated MR
753 signal in the central nervous system. *Magn Reson Med.* 2004;52(5):1052–9.

754

755

$\alpha_{0.6}$ $\alpha_{0.7}$ $\alpha_{0.8}$ $\alpha_{0.9}$ $\alpha_{1.0}$ $\alpha_{1.1}$ $\alpha_{1.2}$
 $\times 10^{-3} \text{ mm}^2/\text{s}$

$K_{0.7}$ $K_{0.65}$ $K_{0.6}$ $K_{0.55}$ $K_{0.5}$ $K_{0.45}$ $K_{0.4}$ $K_{0.35}$ $K_{0.3}$

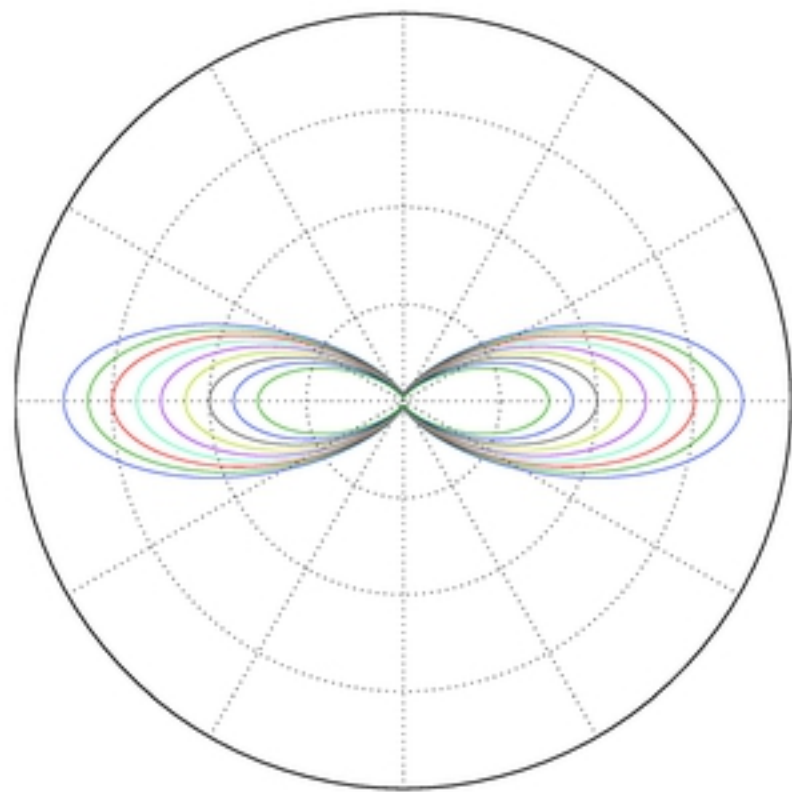
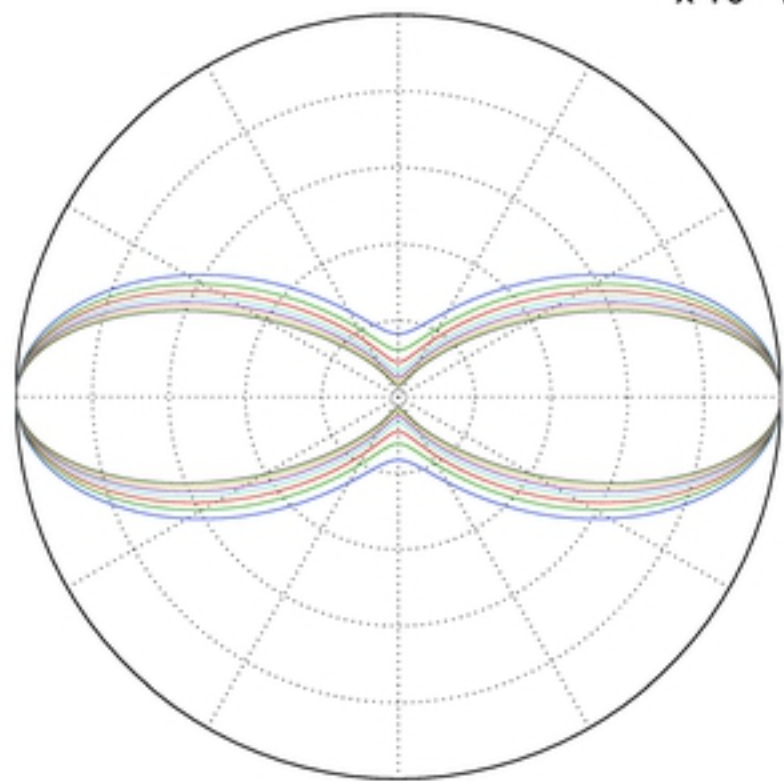


Fig_1

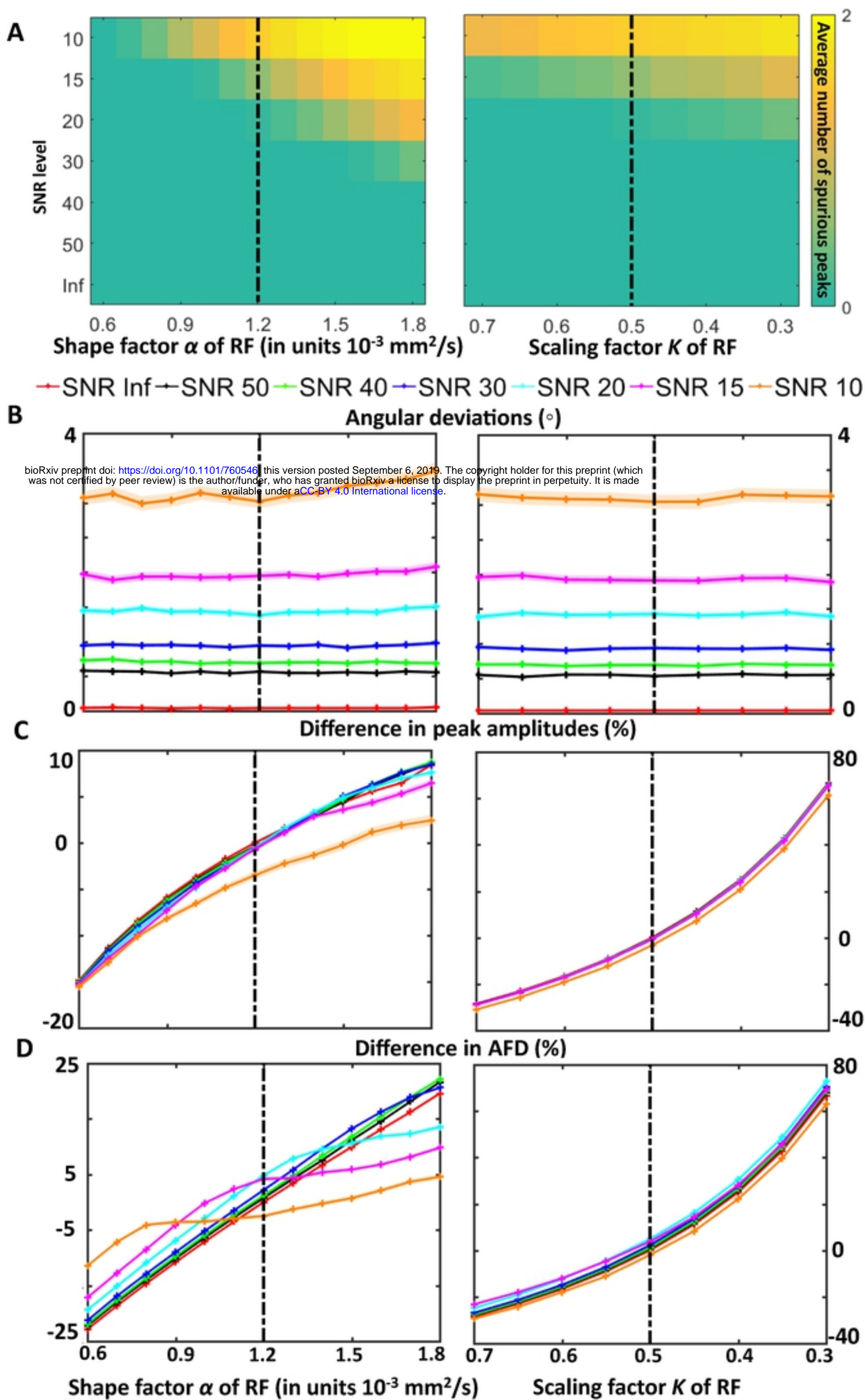


Fig_2

Difference between number of estimated and simulated peaks (Δ)

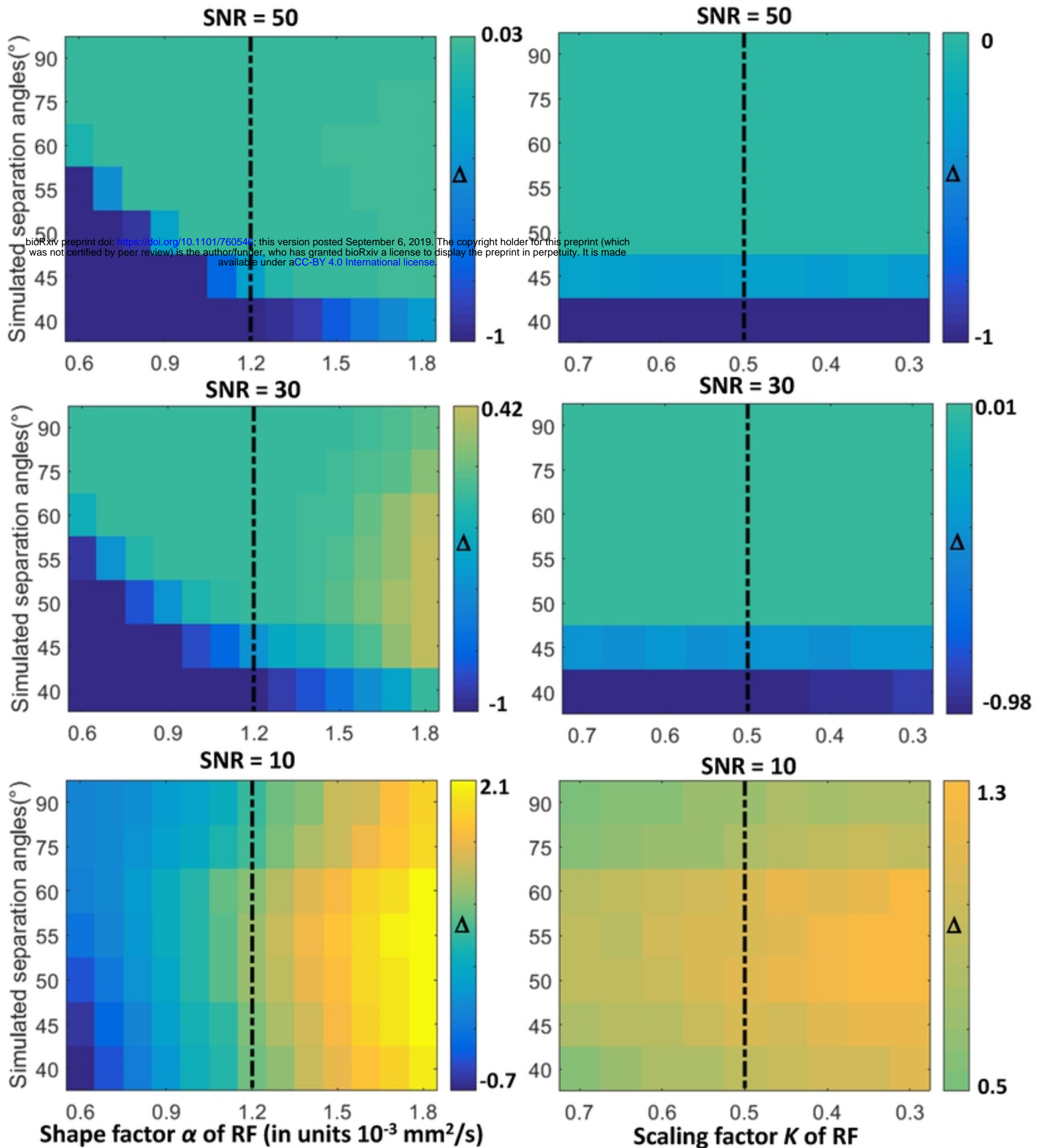


Fig_3

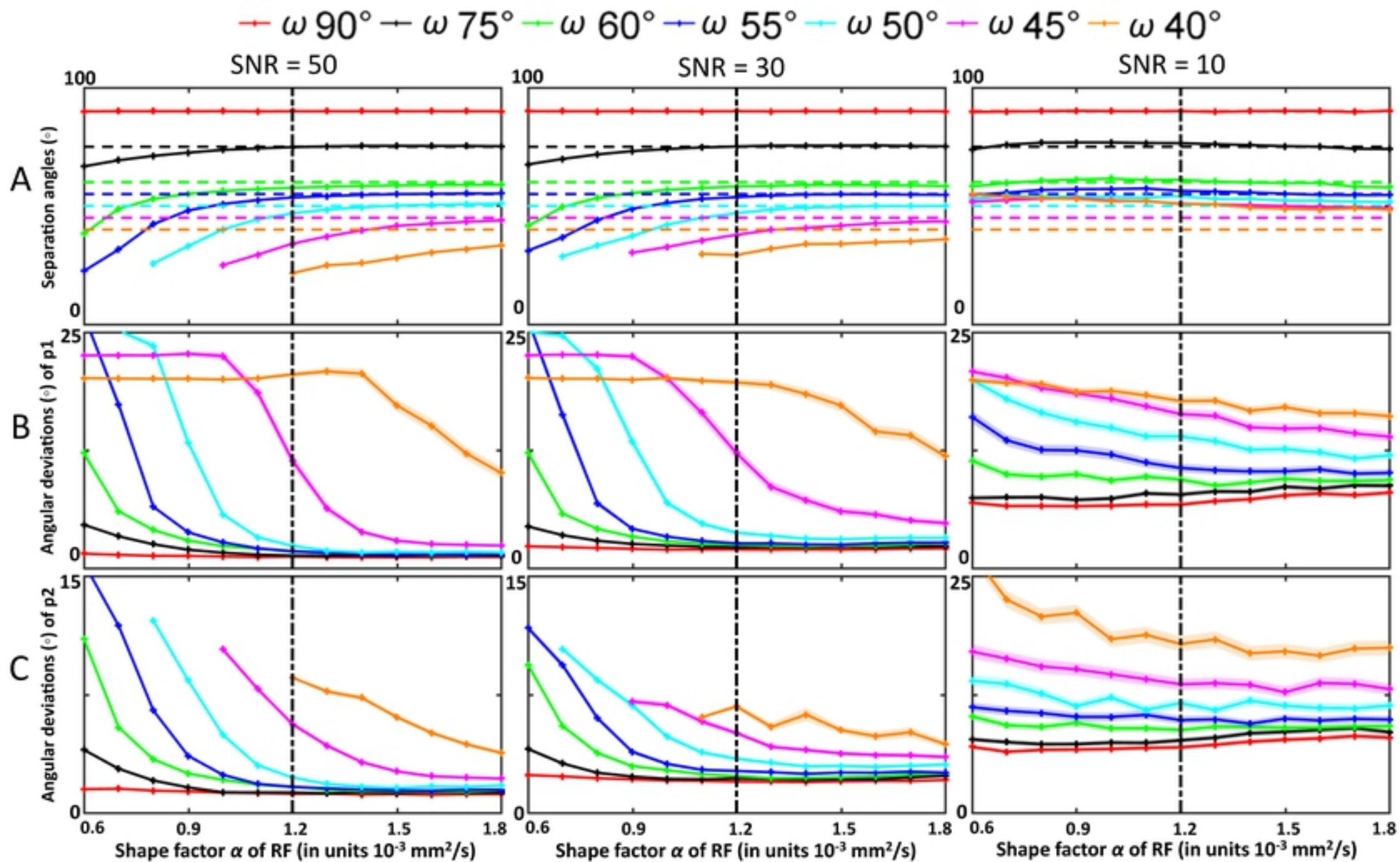


Fig_4

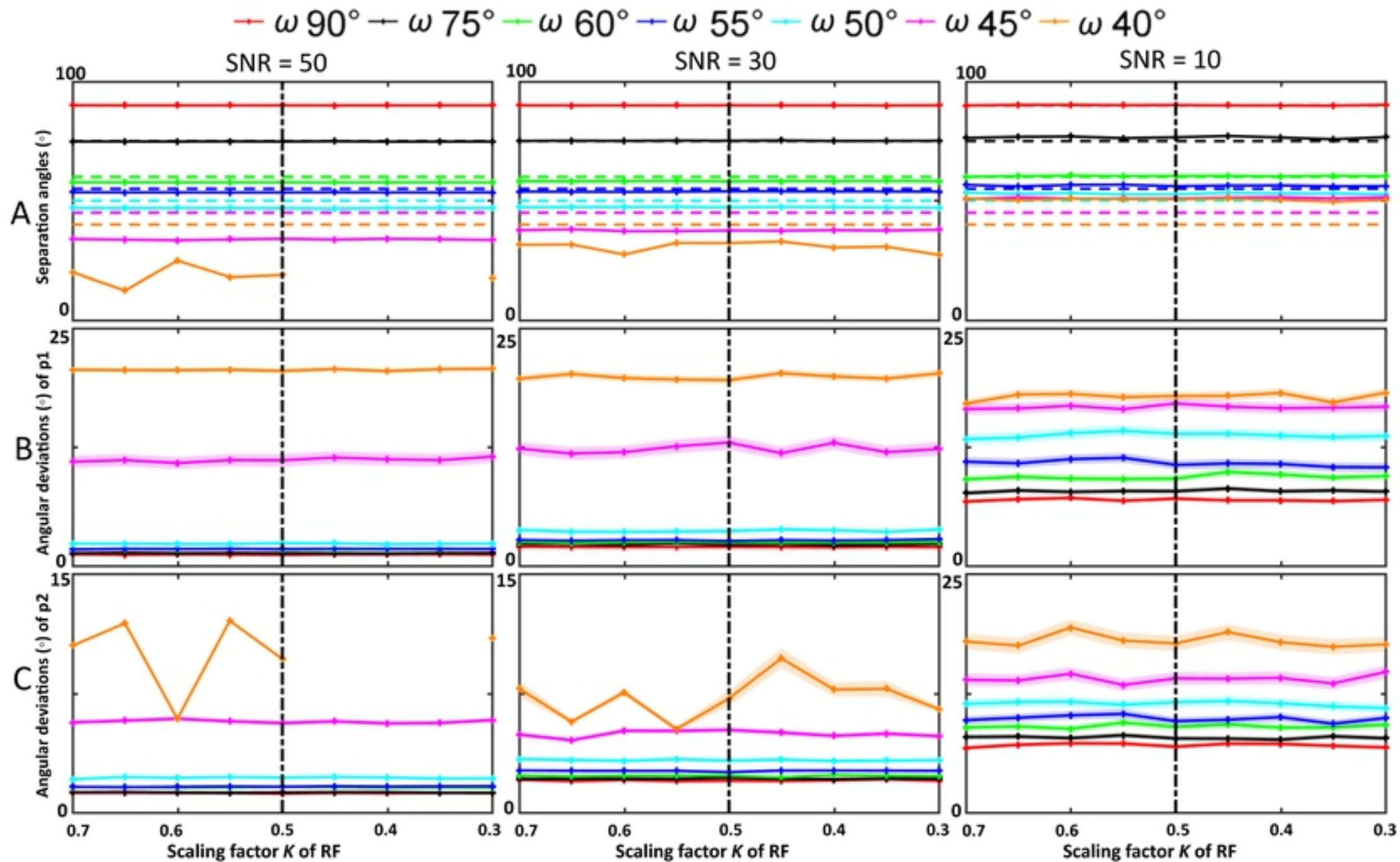


Fig_5

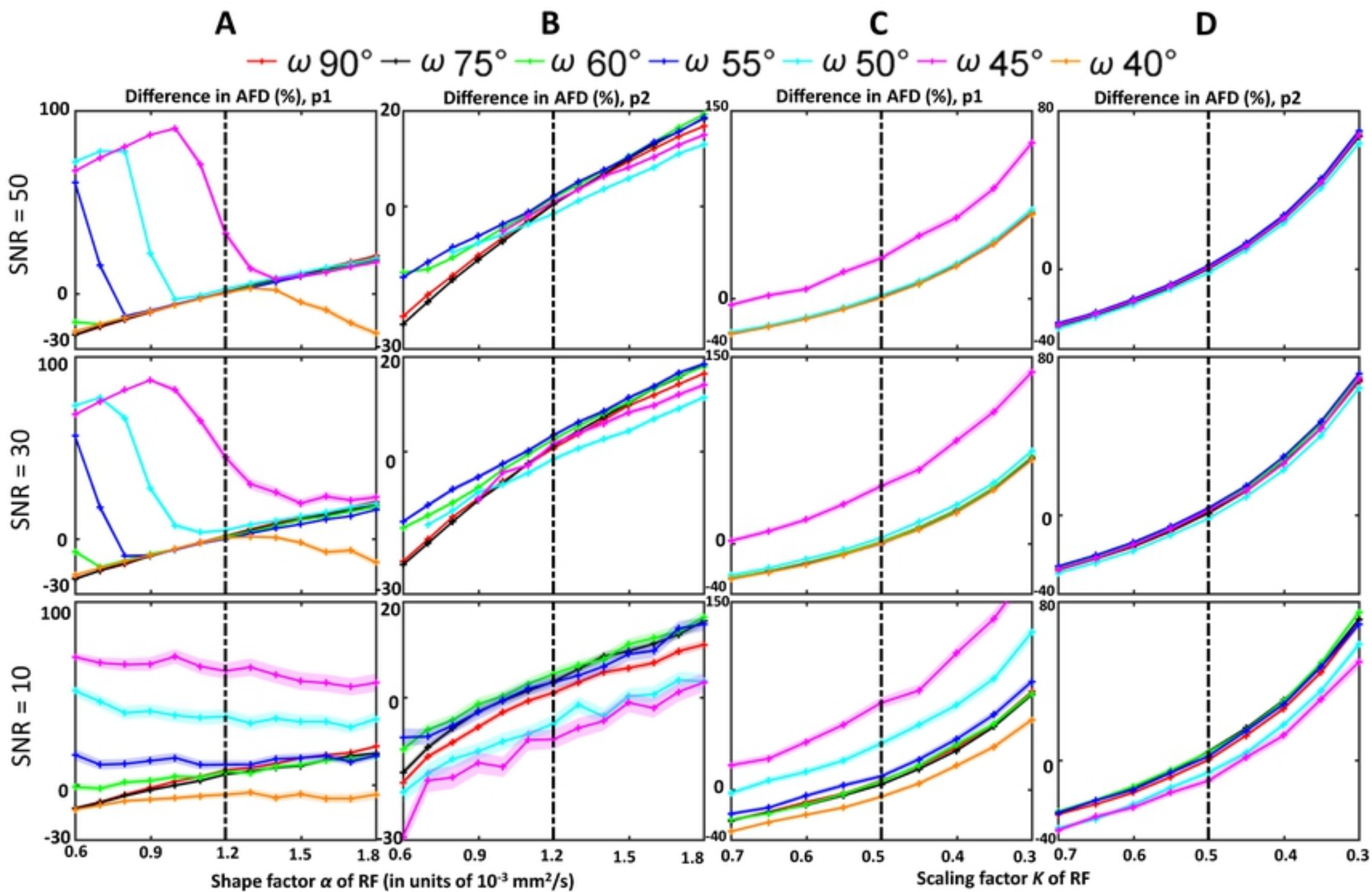
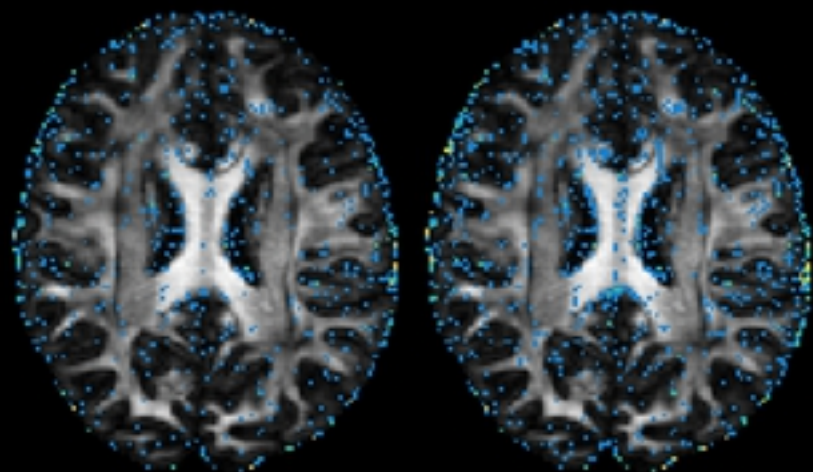


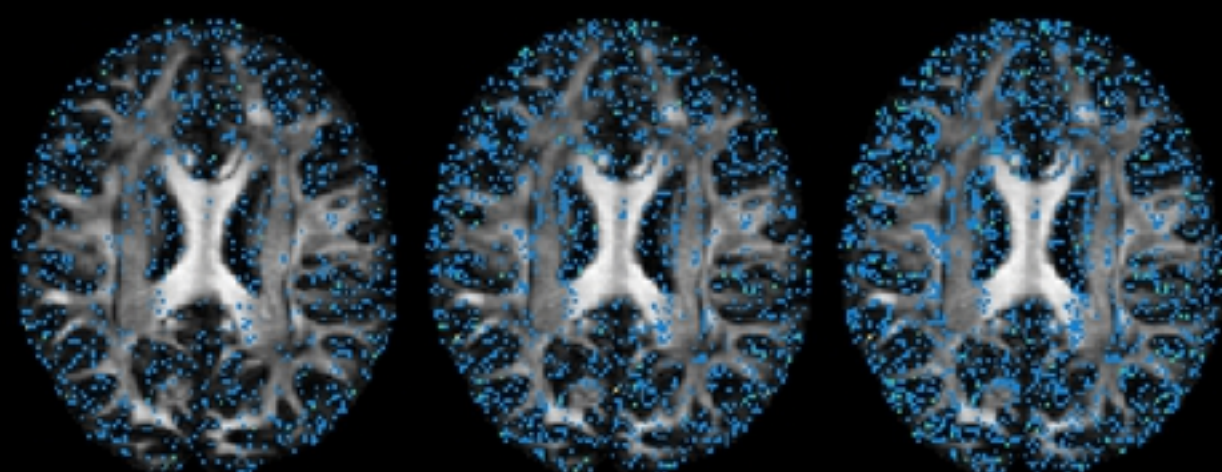
Fig_6

Difference in number of FOD peaks

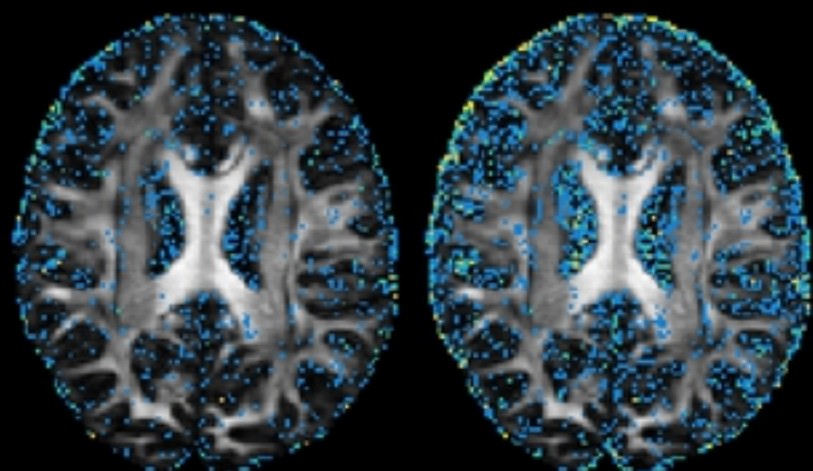


$\Delta K = -0.1$

$\Delta K = -0.2$

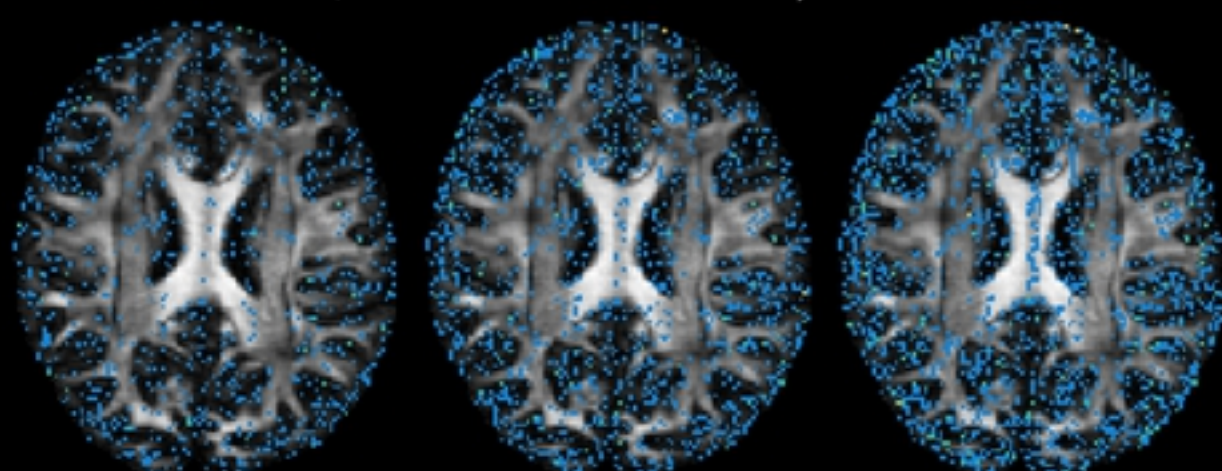


$\Delta\alpha = -0.1 \times 10^{-3} \text{ mm}^2/\text{s}$ $\Delta\alpha = -0.2 \times 10^{-3} \text{ mm}^2/\text{s}$ $\Delta\alpha = -0.3 \times 10^{-3} \text{ mm}^2/\text{s}$



$\Delta K = 0.1$

$\Delta K = 0.2$



$\Delta\alpha = 0.1 \times 10^{-3} \text{ mm}^2/\text{s}$ $\Delta\alpha = 0.2 \times 10^{-3} \text{ mm}^2/\text{s}$ $\Delta\alpha = 0.3 \times 10^{-3} \text{ mm}^2/\text{s}$

Fig_7

Angular deviations of FOD peaks

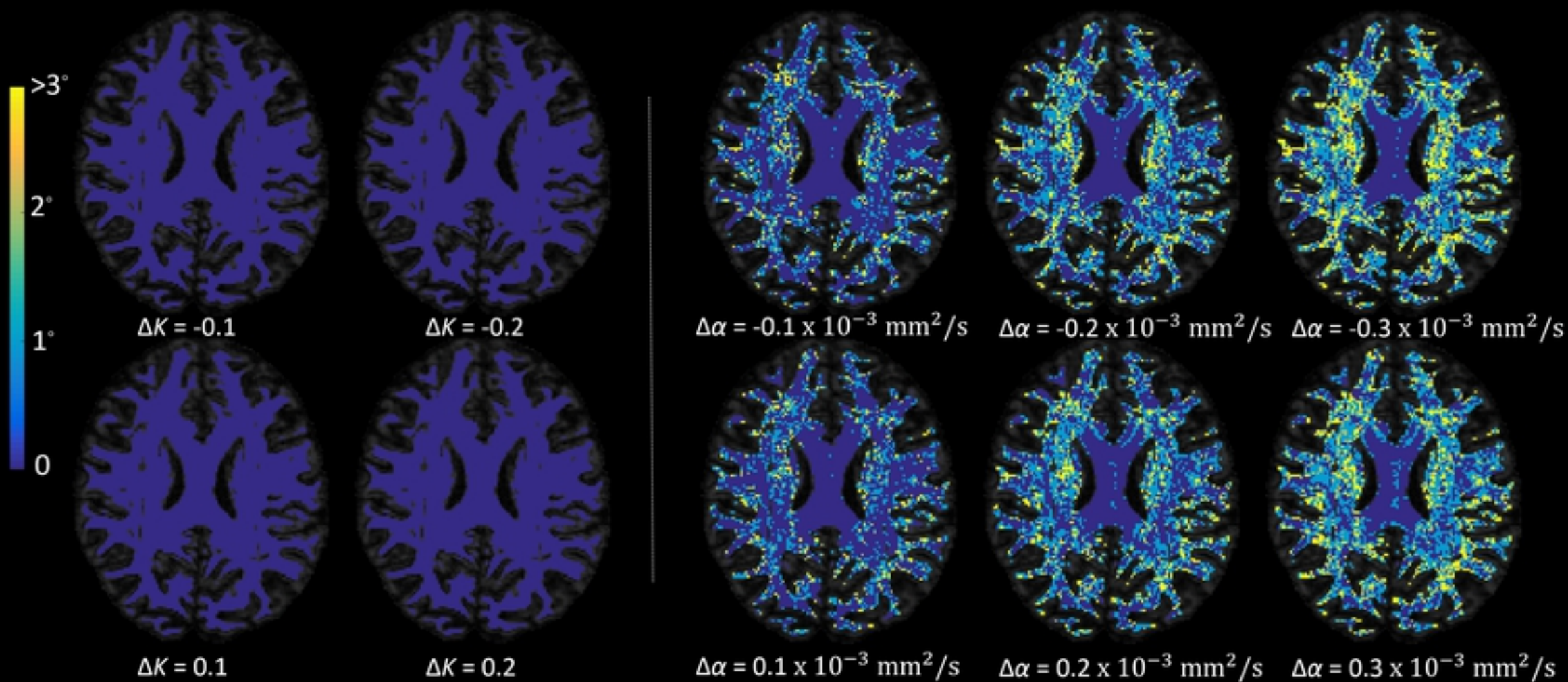


Fig_8

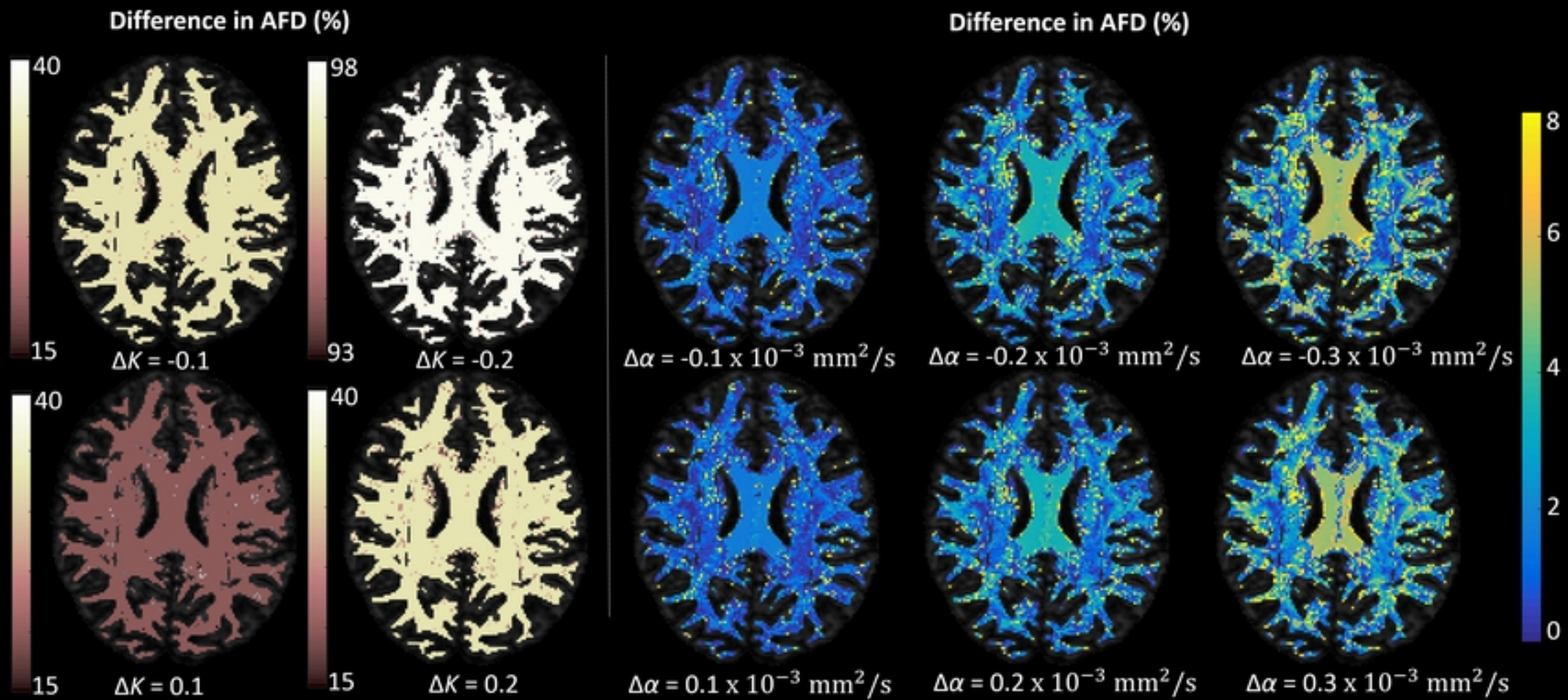


Fig_9

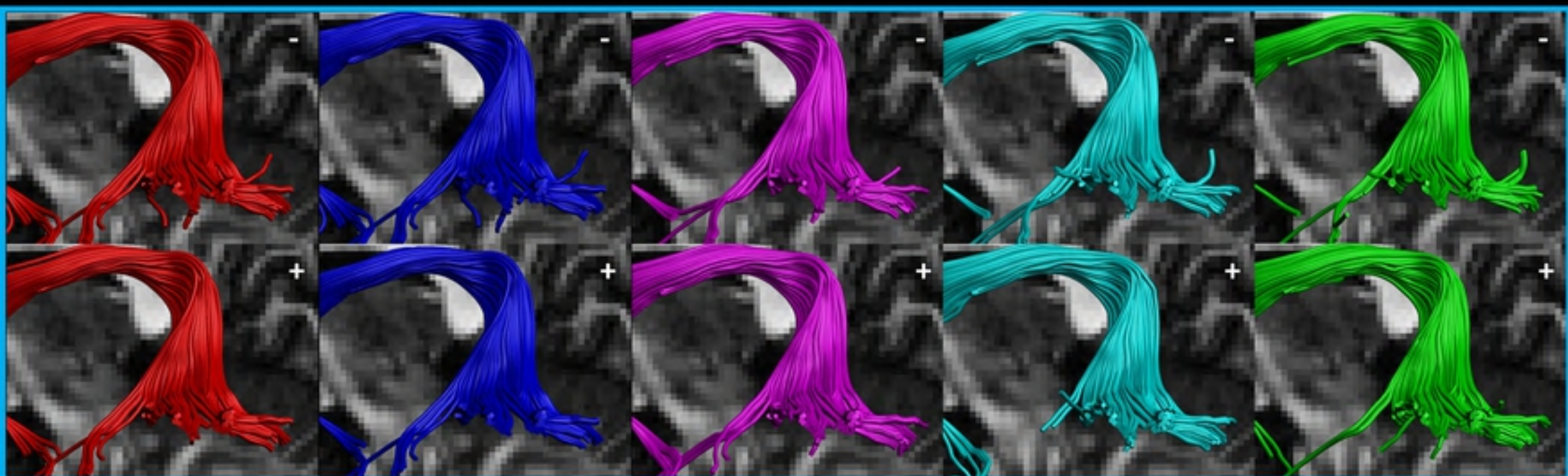
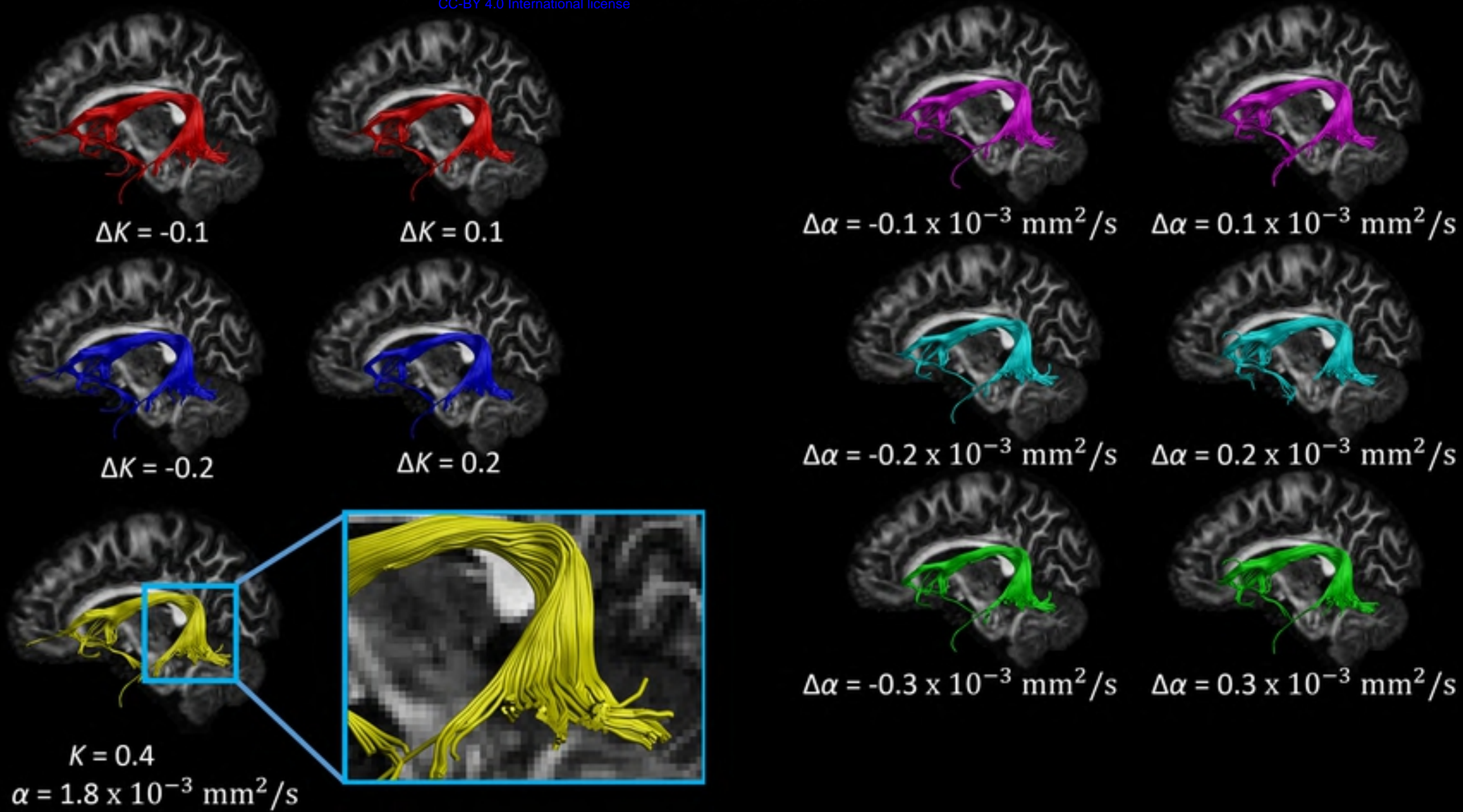
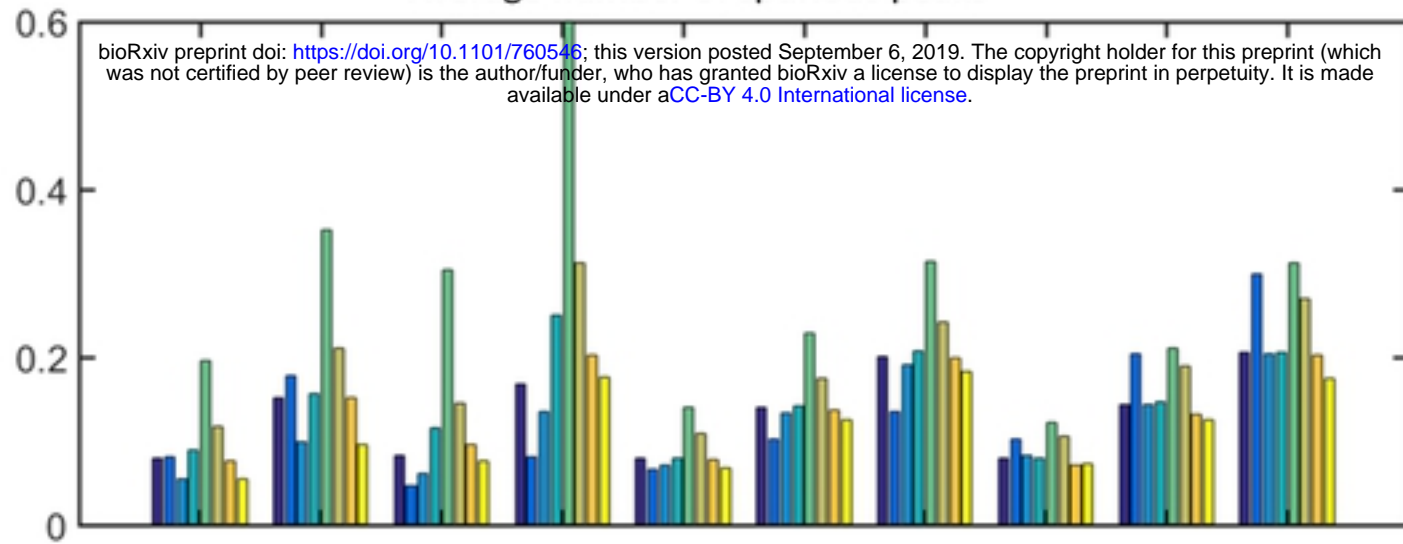
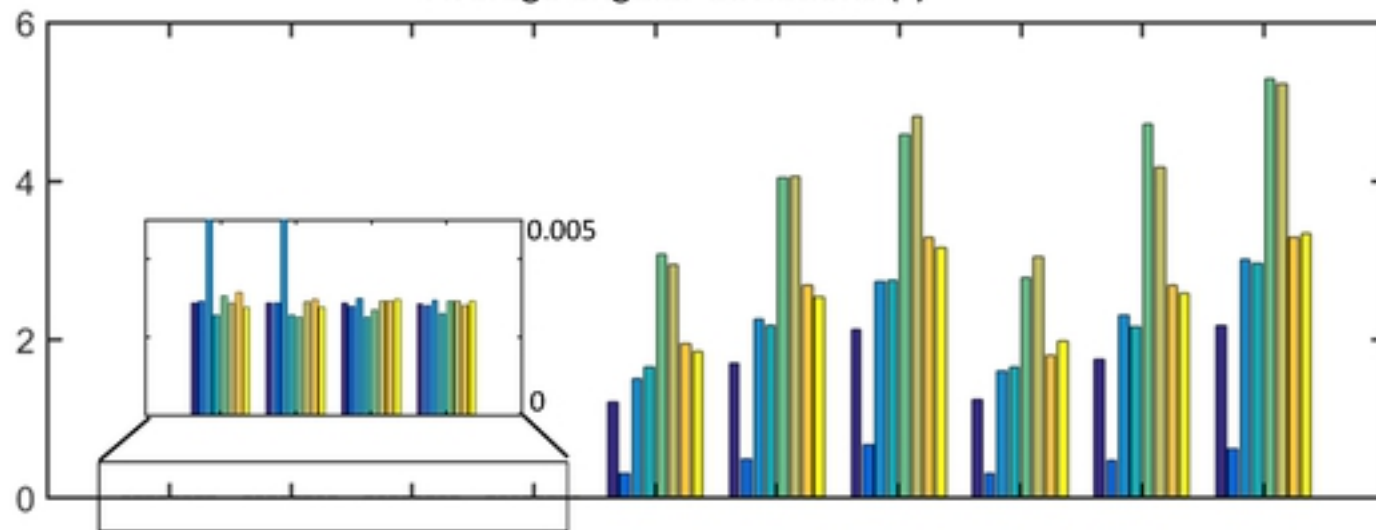


Fig_10

Average number of spurious peaks



Average angular deviations ($^\circ$)



Average difference in AFD (%)

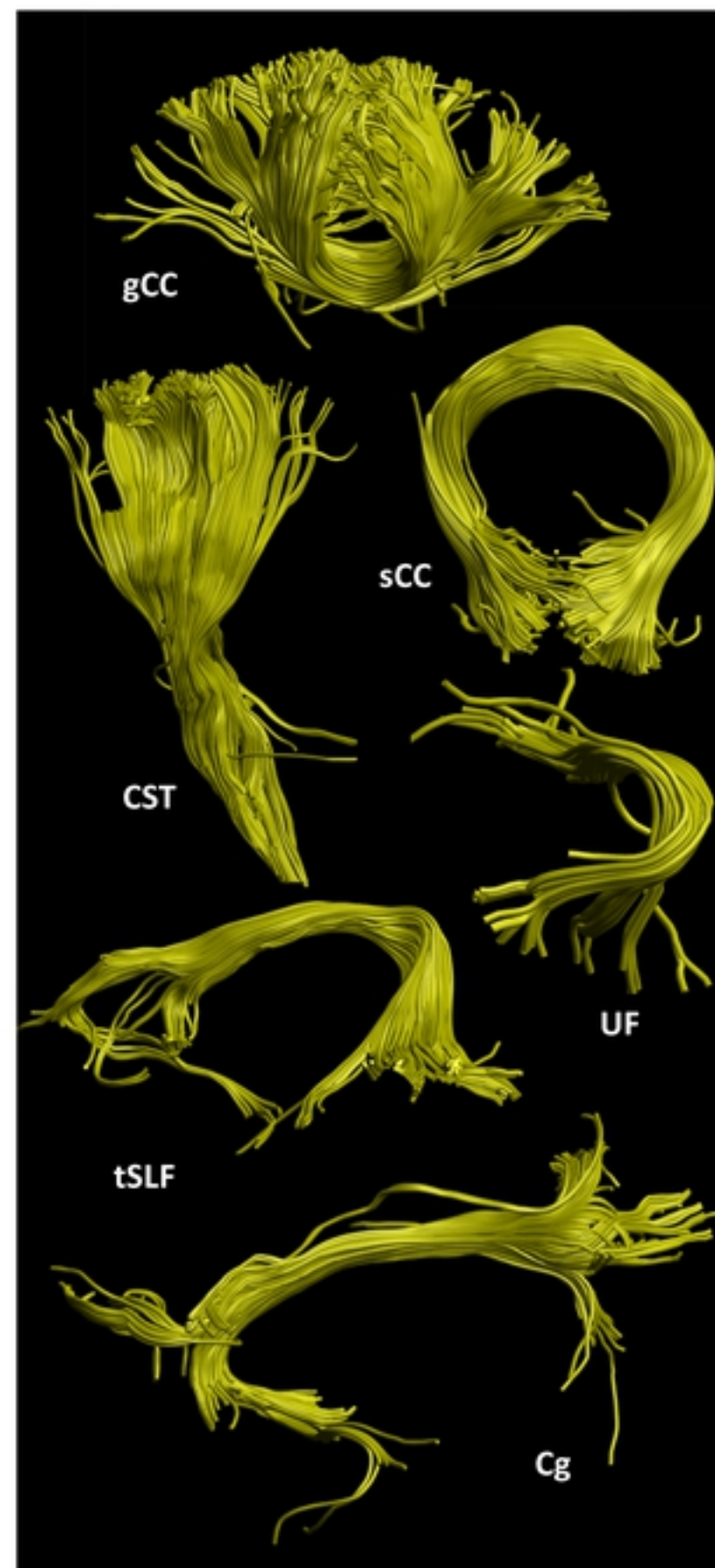
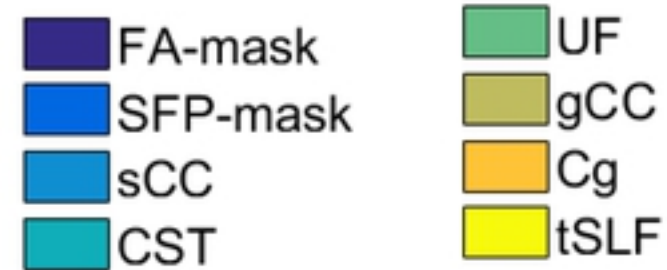
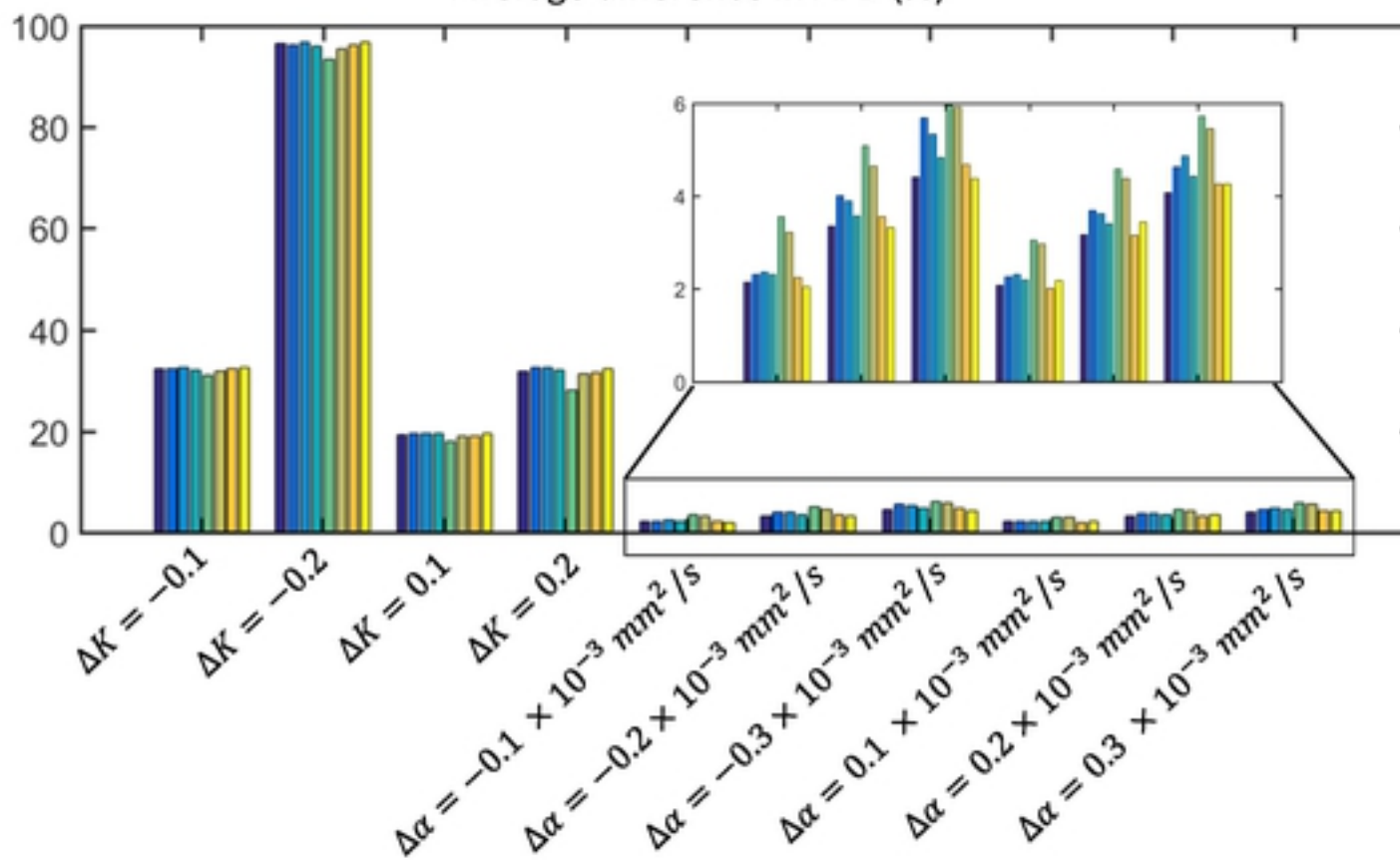


Fig_11